Lagrangian modelling of large deformation induced by progressive failure of sensitive clays with elastoviscoplasticity

Xue Zhang, Daichao Sheng, Scott W Sloan, Jeremy Bleyer

Xue Zhang, Daichao Sheng, Scott W Sloan, Jeremy Bleyer. Lagrangian modelling of large deformation induced by progressive failure of sensitive clays with elastoviscoplasticity. International Journal for Numerical Methods in Engineering, 2017, 112 (8), pp.963-989. ⟨10.1002/nme.5539⟩. ⟨hal-01485340⟩

HAL Id: hal-01485340

https://enpc.hal.science/hal-01485340v1

Submitted on 8 Mar 2017

Lagrangian modelling of large deformation induced by progressive failure of sensitive clays with elastoviscoplasticity

(Dated: Nov 30, 2016)

Xue Zhang[1]*, Daichao Sheng[1], Scott W Sloan[1], Jeremy Bleyer[2]

1. ARC Centre of Excellence for Geotechnical Science and Engineering, University of Newcastle, University Drive, Callaghan, NSW, 2308, Australia
2. Université Paris-Est, Laboratoire Navier, (Ecole des Ponts ParisTech-IFSTTAR-CNRS UMR 8205), 6-8 av. Blaise Pascal, 77420 Champs-Sur-Marne, France

Abstract

This paper presents a Lagrangian formulation of elastoviscoplasticity, based on the Particle Finite Element Method, for progressive failure analysis of sensitive clays. The sensitive clay is represented by an elastoviscoplastic model which is a mixture of the Bingham model, for describing rheological behaviour, and the Tresca model with strain softening for capturing the progressive failure behaviour. The finite element formulation for the incremental elastoviscoplastic analysis is reformulated, through the application of the Hellinger-Reissner variational theorem, as an equivalent optimization program that can be solved efficiently using modern algorithms such as the interior-point method. The recast formulation is then incorporated into the framework of the Particle Finite Element Method for investigating progressive failure problems related to sensitive clays, such as the collapse of a sensitive clay column and the retrogressive failure of a slope in sensitive clays, where extremely large deformation occurs.

Keywords: Sensitive clays; Progressive failure; Elastoviscoplasticity; Strain softening; PFEM; Mathematical programming; SOCP

---

* xue.zhang@uon.edu.au

1. Introduction

Sensitive clay is characterized by a decrease in its shear strength when experiencing plastic deformation. A highly sensitive clay may possess sensitivity, defined as a ratio of the undisturbed shear strength and the remoulded shear strength, of the order of magnitude of a hundred. For example, the reported values of the sensitivity of the clay involved in the 1893 Verdalen landslide and the 2012 Byneset landslide are 300 and 120, respectively [1]. Due to the strong strain-softening behaviour, geostructures built on a layer of sensitive clay often fail in a progressive manner. Moreover, unexpectedly catastrophic failure of the geostructure might also be induced by a small perturbation. Typical examples are the multiple retrogressive slides and spreads in sensitive clays observed in Canada and Scandinavia [2], which occurred suddenly, covered large areas (more than 1 hectare) and were caused by an initially small slope failure.

Reliable prediction of the progressive failure behaviour of sensitive clays is of critical importance. It can provide guidelines for relevant engineering practice, for example construction on sensitive clays, and also assist in minimizing the degree of destruction caused by potential geohazards (such as the fore-mentioned large landslides). Although numerical simulation is a powerful tool for analyzing complex geotechnical problems, robust modelling of the large deformations induced by progressive failure in sensitive clays is still a formidable task. Indeed, a major challenge is the complex behaviour that is typically exhibited by sensitive clays. An undisturbed sensitive clay usually behaves like a solid body, but may change to be a semi-liquid material after being remolded [1]. The transformation between these two states is caused by strain softening. Suitable constitutive models must be capable of describing the rheological behaviour of a sensitive clay, since this is crucial for estimating the run-out distance of landslides [3-5] as well as capturing the strain-softening behaviour that contributes to the phenomenon of progressive failure [2, 6, 7]. Sensitive clays typically undergo extremely large deformation along localized shear zones due to strain-softening. This feature can cause severe mesh distortion when the traditional finite element method is adopted and result in computational difficulties. Additionally, the free-surface evolution induced by extreme deformation also challenges the use of the traditional FEM because of its use of a fixed mesh topology. Recently, some alternative numerical approaches have been proposed for modelling the progressive failure of sensitive clays involving large deformation. Wang *et. al* [8] studied retrogressive and progressive slope failure in sensitive clays using the material point method. Dey *et. al* [9-11] analyzed the spread in sensitive clay slopes due to progressive failure by implementing a strain-softening model into the ABAQUS Coupled Eulerian Lagrangian approach. Although these procedures reproduced the pronounced progressive failure behaviour of sensitive clays, it is notable that classical rate-independent models were utilised. However, ignoring the rheology of sensitive clays may lead to the inaccurate predictions. Analytical approaches, such as shear band propagation approaches [12-16], have also been used to study the progressive failure process in catastrophic landslides in nature. Recent developments in the shear band propagation approach for analyzing catastrophic and progressive failure are summarized in [17].

This paper provides an alternative Lagrangian computational approach for the analysis of progressive failure of sensitive clays involving extremely large deformation. An advanced elastoviscoplastic constitutive relationship, which is a combination of the Bingham model and the Tresca model with strain softening, is adopted for describing their complex behaviour. To solve the resulting elastoviscoplastic problem with strain softening, a generalized incremental Hellinger-Reissner variational theorem [18] is proposed which recasts the associated governing equations into an equivalent min-max program. After finite element discretisation, the resulting problem can be converted into a standard second-order cone programming problem which may be solved efficiently using modern optimization algorithms (for example, the primal-dual interior point method [19]). Typical advantages of such a solution strategy include the possibility of analyzing the existence, uniqueness, sensitivity and stability of the solution [20], the natural treatment of the singularities in the Mohr-Coulomb and Drucker-Prager yield criteria [21-23], the straightforward extension from single-surface plasticity to multi-surface plasticity [21], and the straightforward implementation of contact between deformable and rigid bodies [24, 25]. The proposed solution algorithm is incorporated into the framework of the Particle Finite Element Method (PFEM) [26-28] for handling large deformation. The PFEM is a novel continuum approach suitable for simulating problems involving both solid-like and fluid-like behaviour [27, 29, 30]. It makes use of particles to represent the material, as in meshfree particle methods, but solves the governing equations via a standard finite element procedure. Consequently, the PFEM inherits both the solid mathematical foundation of the traditional FEM as well as the capability of meshfree particle methods for handling extremely large deformation and free-surface evolution.

The paper is organized as follows. Section 2 presents the governing equations for dynamic analysis of an elastoviscoplastic problem. An incremental mixed variational principle is then proposed in Section 3 for recasting the governing equations into a min-max problem. Finite element discretisation is performed in Section 4, and the Particle Finite Element Method is described briefly in Section 5. Numerical examples are given in Section 6, before conclusions are drawn in Section 7.

2. Governing equations for elastoviscoplasticity

Consider a medium with volume Ω and surface $\Gamma = \Gamma_{\mathrm{u}} \bigcup \Gamma_{\mathrm{t}}$, where Γ_{u} and Γ_{t} are the kinematic and traction boundaries, respectively. The partition of the surface obeys the constraint $\Gamma_{\mathrm{u}} \bigcap \Gamma_{\mathrm{t}} = \varnothing$ where $\varnothing$ is a null set. The momentum conservation equation, the kinematic equations for displacement gradients, and the corresponding boundary conditions read

$$\nabla^{\mathrm{T}}\boldsymbol{\sigma} + \mathbf{b} = \rho\ddot{\mathbf{u}} \quad \text{in}\,\Omega \tag{1}$$

$$\boldsymbol{\varepsilon} = \nabla^{\mathrm{T}}\mathbf{u} \quad \text{in}\,\Omega \tag{2}$$

$$\mathbf{u} = \bar{\mathbf{u}} \quad \text{on}\,\Gamma_{\mathrm{u}} \tag{3}$$

$$\mathbf{N}^{\mathrm{T}}\boldsymbol{\sigma} = \bar{\mathbf{t}} \quad \text{on}\,\Gamma_{\mathrm{t}} \tag{4}$$

where $\boldsymbol{\sigma}$ and $\boldsymbol{\varepsilon}$ are the Cauchy stress and the strain, $\mathbf{b}$ is the body force, $\mathbf{u}$ is the displacement, $\bar{\mathbf{u}}$ and $\bar{\mathbf{t}}$ are the prescribed displacements and external tractions, $\mathbf{N}$ consists of components of the outward normal to the boundary Γ_{t}, and ∇ is the usual linear operator taking the form of

$$\nabla^{\mathrm{T}} = \begin{bmatrix} \dfrac{\partial}{\partial x} & 0 & 0 & \dfrac{\partial}{\partial y} \\ 0 & \dfrac{\partial}{\partial y} & 0 & \dfrac{\partial}{\partial x} \end{bmatrix} \tag{5}$$

in a plane-strain case. A superposed dot represents differentiation with respect to time.

Assuming the material is elastoviscoplastic, the total strain rate $\dot{\boldsymbol{\varepsilon}}$ can then be split into an elastic strain rate $\dot{\boldsymbol{\varepsilon}}^{\mathrm{e}}$ and a viscoplastic strain rate $\dot{\boldsymbol{\varepsilon}}^{\mathrm{vp}}$

$$\dot{\boldsymbol{\varepsilon}} = \dot{\boldsymbol{\varepsilon}}^{\mathrm{e}} + \dot{\boldsymbol{\varepsilon}}^{\mathrm{vp}} \tag{6}$$

The elastic strain rate is determined through Hook’s law as

$$\dot{\boldsymbol{\varepsilon}}^{\mathrm{e}} = \mathbb{C}\dot{\boldsymbol{\sigma}} \tag{7}$$

where $\mathbb{C}$ is the elastic compliance matrix. The material is elastic if the stress state is inside the yield domain, namely

$$F(\boldsymbol{\sigma}) < 0 \Rightarrow \dot{\boldsymbol{\varepsilon}}^{\mathrm{vp}} = \mathbf{0} \tag{8}$$

where F is the yield function. In contrast, stress states satisfying $F(\boldsymbol{\sigma}) \geq 0$ lead to a viscoplastic strain rate. The classical Bingham model is utilized in this paper for describing the rheological properties of the sensitive clay. Despite its simple form, it performs well for approximating the plastic flow behaviour of these soils, especially Canadian clays [5]. The total stress thus is rewritten as

$$\boldsymbol{\sigma} = \boldsymbol{\tau} + \eta \dot{\boldsymbol{\varepsilon}}^{\mathrm{vp}} \tag{9}$$

where η is the viscosity coefficient, $\boldsymbol{\tau}$ is the stress lying on the boundary of F so that $F(\boldsymbol{\tau}) = 0$, and the quantity $\boldsymbol{\sigma} - \boldsymbol{\tau}$ is called the overstress. The viscoplastic strain rate is also normal to the yield surface at $\boldsymbol{\tau}$:

$$\dot{\boldsymbol{\varepsilon}}^{\mathrm{vp}} = \dot{\lambda} \nabla_{\boldsymbol{\tau}} F(\boldsymbol{\tau}) \tag{10}$$

where $\dot{\lambda}$ is the rate of the non-negative plastic multiplier and $\nabla_{\boldsymbol{\tau}}$ is the gradient operator. It is clear that the above elastoviscoplastic model reduces to the classical elastoplastic model in the limiting case of $\eta = 0$.

Laboratory tests show that the undrained shear strength of a sensitive clay decreases with increasing plastic shear strain. For materials exhibiting softening/hardening behaviour, the yield criterion function is expressed by $F(\boldsymbol{\tau}, \kappa) = 0$, where κ is a set of hardening/softening variables which relate to the viscoplastic strain in the form of

$$\kappa = H(\boldsymbol{\varepsilon}^{vp}) \tag{11}$$

Specifically, for the Tresca yield criterion, we have

$$F(\boldsymbol{\sigma},\kappa)=\sqrt{(\sigma_{xx}-\sigma_{yy})^2+4\sigma_{xy}^2}-2c_{\mathrm{u}}(\kappa) \tag{12}$$

where cohesion softening is adopted to capture the basic post-failure behaviour. Following [31, 32], strain-softening is accounted for by reducing the cohesion c_{u} using a bilinear function (Figure 1) of the equivalent deviatoric plastic strain, $\kappa=\int\dot{\kappa}\mathrm{d}t$, where $\dot{\kappa}=\sqrt{0.5\dot{e}_{ij}^{\mathrm{vp}}\dot{e}_{ij}^{\mathrm{vp}}}$ and $\dot{e}_{ij}^{\mathrm{vp}}$ is the rate of deviatoric viscoplastic strain tensor given by

$$\dot{e}_{ij}^{\mathrm{vp}}=\dot{\varepsilon}_{ij}^{\mathrm{vp}}-\frac{1}{3}\dot{\varepsilon}_{kk}^{\mathrm{vp}}\delta_{ij} \tag{13}$$

in which δ_{ij} is the Kronecker delta.

3. Variational principle

3.1 Hellinger-Reissner variational principle

The Hellinger-Reissner (HR) variational principle is of a mixed kind. Unlike the principle of minimum potential energy, in which displacements are considered as the only master field, the Hellinger-Reissner variational principle treats both the displacements and the stresses as the master fields [18].

For an elastostatic boundary-value problem, the Hellinger-Reissner functional [18] may be expressed as

$$\Pi(\boldsymbol{\sigma},\mathbf{u})=\int_{\Omega}(-\frac{1}{2}\boldsymbol{\sigma}^{\mathrm{T}}\mathbb{C}\boldsymbol{\sigma}+\boldsymbol{\sigma}^{\mathrm{T}}\mathbf{S}^{\mathrm{T}}\mathbf{u})\mathrm{d}\Omega-\int_{\Omega}\mathbf{b}^{\mathrm{T}}\mathbf{u}\mathrm{d}\Omega-\int_{\Gamma_{\mathrm{t}}}\overline{\mathbf{t}}^{\mathrm{T}}\mathbf{u}\mathrm{d}\Gamma \tag{14}$$

The stationary value for the Hellinger-Reissner functional cannot be shown to be an extremum. Instead, the point obtained by $\delta\Pi(\boldsymbol{\sigma},\mathbf{u})=0$ is a saddle point and, consequently, the problem becomes one of a min-max optimisation:

$$\min_{\mathbf{u}} \max_{\boldsymbol{\sigma}} \int_\Omega (-\frac{1}{2}\boldsymbol{\sigma}^{\mathrm{T}}\mathbb{C}\boldsymbol{\sigma} + \boldsymbol{\sigma}^{\mathrm{T}}\mathbf{S}^{\mathrm{T}}\mathbf{u})\mathrm{d}\Omega - \int_\Omega \mathbf{b}^{\mathrm{T}}\mathbf{u}\mathrm{d}\Omega - \int_{\Gamma_t} \bar{\mathbf{t}}^{\mathrm{T}}\mathbf{u}\mathrm{d}\Gamma \tag{15}$$

where the internal work is maximised with respect to the stresses and the total potential energy is minimised with respect to the displacements.

3.2 Generalised Hellinger-Reissner variational principle

A generalised Hellinger-Reissner variational principle is proposed for incremental analysis of elastoviscoplasticity. The governing equations summarised in section 2 are first discretized in time using the standard θ-method. Details of the time discretisation, as well as the resulting incremental equations, are documented in Appendix A.

We present here the generalized incremental Hellinger-Reissner variational principle for incremental elasto-viscoplastic analysis. As for elastostatics, the principle is expressed in the form of a min-max program:

$$\begin{aligned}
\min_{\Delta\mathbf{u}} \max_{(\boldsymbol{\sigma},\boldsymbol{\tau},\mathbf{r})_{\mathrm{n+1}}} \quad & -\frac{1}{2}\int_\Omega \Delta\boldsymbol{\sigma}^{\mathrm{T}}\mathbb{C}\Delta\boldsymbol{\sigma}\mathrm{d}\Omega + \int_\Omega \boldsymbol{\sigma}_{\mathrm{n+1}}^{\mathrm{T}}\nabla^{\mathrm{T}}(\Delta\mathbf{u})\mathrm{d}\Omega + \int_\Omega \frac{1-\theta_1}{\theta_1}\boldsymbol{\sigma}_{\mathrm{n}}^{\mathrm{T}}\nabla^{\mathrm{T}}(\Delta\mathbf{u})\mathrm{d}\Omega \\
& -\frac{1}{2}\int_\Omega \mathbf{r}_{\mathrm{n+1}}^{\mathrm{T}}\frac{\Delta t^2}{\tilde{\rho}}\mathbf{r}_{\mathrm{n+1}}\mathrm{d}\Omega + \int_\Omega \mathbf{r}_{\mathrm{n+1}}^{\mathrm{T}}\Delta\mathbf{u}\mathrm{d}\Omega \\
& -\frac{1}{2}\int_\Omega (\Delta\boldsymbol{\sigma}-\Delta\boldsymbol{\tau})^{\mathrm{T}}\frac{\theta_3\Delta t}{\eta}(\Delta\boldsymbol{\sigma}-\Delta\boldsymbol{\tau})\mathrm{d}\Omega - \int_\Omega \Delta\boldsymbol{\sigma}^{\mathrm{T}}\frac{\Delta t}{\eta}(\boldsymbol{\sigma}_{\mathrm{n}}-\boldsymbol{\tau}_{\mathrm{n}})\mathrm{d}\Omega \\
& +\int_\Omega (\boldsymbol{\sigma}_{\mathrm{n}}-\boldsymbol{\tau}_{\mathrm{n}})^{\mathrm{T}}\frac{\Delta t}{\eta}\Delta\boldsymbol{\tau}\mathrm{d}\Omega - \int_\Omega \tilde{\mathbf{b}}^{\mathrm{T}}\Delta\mathbf{u}\mathrm{d}\Omega - \int_{\Gamma_t} \tilde{\mathbf{t}}^{\mathrm{T}}\Delta\mathbf{u}\mathrm{d}\Gamma \\
\text{subject to} \quad & F(\boldsymbol{\tau}_{\mathrm{n+1}}) \le 0
\end{aligned} \tag{16}$$

where **r** is a set of variables that can be interpreted as dynamic forces. To illustrate the equivalence between the program (16) and the incremental form of the governing equations presented in Appendix A, the Karush-Kuhn-Tucker (KKT) optimality conditions associated with (16) are now derived. Following [23, 33], the inequality constraint is first converted into an equality by adding a positively-restricted variable $s_{\mathrm{n+1}}$. Then, the inequality on $s_{\mathrm{n+1}}$ is represented by introducing a penalty term in the objective function:

$$\begin{aligned}
\min_{\Delta\mathbf{u}}\ \max_{(\boldsymbol{\sigma},\boldsymbol{\tau},\mathbf{r})_{n+1}}\quad & -\frac{1}{2}\int_{\Omega}\Delta\boldsymbol{\sigma}^{\mathrm{T}}\mathbb{C}\Delta\boldsymbol{\sigma}\mathrm{d}\Omega+\int_{\Omega}\boldsymbol{\sigma}_{n+1}^{\mathrm{T}}\nabla^{\mathrm{T}}(\Delta\mathbf{u})\mathrm{d}\Omega+\int_{\Omega}\frac{1-\theta_1}{\theta_1}\boldsymbol{\sigma}_{n}^{\mathrm{T}}\nabla^{\mathrm{T}}(\Delta\mathbf{u})\mathrm{d}\Omega \\
& -\frac{1}{2}\int_{\Omega}\mathbf{r}_{n+1}^{\mathrm{T}}\frac{\Delta t^2}{\tilde{\rho}}\mathbf{r}_{n+1}\mathrm{d}\Omega+\int_{\Omega}\mathbf{r}_{n+1}^{\mathrm{T}}\Delta\mathbf{u}\mathrm{d}\Omega \\
& -\frac{1}{2}\int_{\Omega}(\Delta\boldsymbol{\sigma}-\Delta\boldsymbol{\tau})^{\mathrm{T}}\frac{\theta_3\Delta t}{\eta}(\Delta\boldsymbol{\sigma}-\Delta\boldsymbol{\tau})\mathrm{d}\Omega-\int_{\Omega}\Delta\boldsymbol{\sigma}^{\mathrm{T}}\frac{\Delta t}{\eta}(\boldsymbol{\sigma}_{n}-\boldsymbol{\tau}_{n})\mathrm{d}\Omega \\
& +\int_{\Omega}(\boldsymbol{\sigma}_{n}-\boldsymbol{\tau}_{n})^{\mathrm{T}}\frac{\Delta t}{\eta}\Delta\boldsymbol{\tau}\mathrm{d}\Omega-\int_{\Omega}\tilde{\mathbf{b}}^{\mathrm{T}}\Delta\mathbf{u}\mathrm{d}\Omega-\int_{\Gamma_t}\tilde{\mathbf{t}}^{\mathrm{T}}\Delta\mathbf{u}\mathrm{d}\Gamma+\int_{\Omega}\mu\ln s_{n+1}\mathrm{d}\Omega \\
\text{subject to}\quad & F(\boldsymbol{\tau}_{n+1})+s_{n+1}=0
\end{aligned}\tag{17}$$

where μ is a sufficiently small positive constant. The penalty term $\mu\ln s_{n+1}$ in the objective function imposes the non-negativity requirement on s_{n+1} naturally, and is known as a logarithmic barrier function. The Lagrangian associated with program (17) is

$$\begin{aligned}
& \mathcal{L}(\Delta\mathbf{u},\boldsymbol{\sigma}_{n+1},\boldsymbol{\tau}_{n+1},\mathbf{r}_{n+1},\Delta\lambda,s_{n+1}) \\
& =-\frac{1}{2}\int_{\Omega}\Delta\boldsymbol{\sigma}^{\mathrm{T}}\mathbb{C}\Delta\boldsymbol{\sigma}\mathrm{d}\Omega+\int_{\Omega}\boldsymbol{\sigma}_{n+1}^{\mathrm{T}}\nabla^{\mathrm{T}}(\Delta\mathbf{u})\mathrm{d}\Omega+\int_{\Omega}\frac{1-\theta_1}{\theta_1}\boldsymbol{\sigma}_{n}^{\mathrm{T}}\nabla^{\mathrm{T}}(\Delta\mathbf{u})\mathrm{d}\Omega \\
& \quad -\frac{1}{2}\int_{\Omega}\mathbf{r}_{n+1}^{\mathrm{T}}\frac{\Delta t^2}{\tilde{\rho}}\mathbf{r}_{n+1}\mathrm{d}\Omega+\int_{\Omega}\mathbf{r}_{n+1}^{\mathrm{T}}\Delta\mathbf{u}\mathrm{d}\Omega-\frac{1}{2}\int_{\Omega}(\Delta\boldsymbol{\sigma}-\Delta\boldsymbol{\tau})^{\mathrm{T}}\frac{\theta_3\Delta t}{\eta}(\Delta\boldsymbol{\sigma}-\Delta\boldsymbol{\tau})\mathrm{d}\Omega \\
& \quad -\int_{\Omega}\Delta\boldsymbol{\sigma}^{\mathrm{T}}\frac{\Delta t}{\eta}(\boldsymbol{\sigma}_{n}-\boldsymbol{\tau}_{n})\mathrm{d}\Omega+\int_{\Omega}(\boldsymbol{\sigma}_{n}-\boldsymbol{\tau}_{n})^{\mathrm{T}}\frac{\Delta t}{\eta}\Delta\boldsymbol{\tau}\mathrm{d}\Omega-\int_{\Omega}\tilde{\mathbf{b}}^{\mathrm{T}}\Delta\mathbf{u}\mathrm{d}\Omega-\int_{\Gamma_t}\tilde{\mathbf{t}}^{\mathrm{T}}\Delta\mathbf{u}\mathrm{d}\Gamma \\
& \quad +\int_{\Omega}\mu\ln s_{n+1}\mathrm{d}\Omega-\int_{\Omega}\Delta\lambda(F(\boldsymbol{\tau}_{n+1})+s_{n+1})\mathrm{d}\Omega
\end{aligned}\tag{18}$$

The KKT optimality conditions are found by differentiating the above Lagrangian with respect to the optimisation variables, namely:

$$\frac{\partial\mathcal{L}}{\partial\Delta\mathbf{u}}=\begin{cases}\nabla^{\mathrm{T}}\boldsymbol{\sigma}_{n+1}+\dfrac{1-\theta_1}{\theta_1}\nabla^{\mathrm{T}}\boldsymbol{\sigma}_{n}+\mathbf{r}_{n+1}-\tilde{\mathbf{b}}=\mathbf{0} & \text{in }\Omega \\ \mathbf{N}^{\mathrm{T}}(\boldsymbol{\sigma}_{n+1}+\dfrac{1-\theta_1}{\theta_1}\boldsymbol{\sigma}_{n})=\tilde{\mathbf{t}} & \text{on }\Gamma_t\end{cases}\tag{19}$$

$$\frac{\partial\mathcal{L}}{\partial\boldsymbol{\sigma}_{n+1}}=\nabla^{\mathrm{T}}(\Delta\mathbf{u})-\mathbb{C}\Delta\boldsymbol{\sigma}-\frac{\theta_3\Delta t}{\eta}(\Delta\boldsymbol{\sigma}-\Delta\boldsymbol{\tau})-\frac{\Delta t}{\eta}(\boldsymbol{\sigma}_{n}-\boldsymbol{\tau}_{n})=\mathbf{0}\quad\text{in }\Omega\tag{20}$$

$$\frac{\partial \mathcal{L}}{\partial \boldsymbol{\tau}_{n+1}} = \frac{\theta_3 \Delta t}{\eta}(\Delta\boldsymbol{\sigma} - \Delta\boldsymbol{\tau}) + \frac{\Delta t}{\eta}(\boldsymbol{\sigma}_n - \boldsymbol{\tau}_n) - \Delta\lambda \nabla_G F(\boldsymbol{\tau}_{n+1}) = \mathbf{0} \quad \text{in } \Omega \tag{21}$$

$$\frac{\partial \mathcal{L}}{\partial \mathbf{r}_{n+1}} = \frac{\Delta t^2}{\tilde{\rho}} \mathbf{r}_{n+1} - \Delta\mathbf{u} = \mathbf{0} \quad \text{in } \Omega \tag{22}$$

$$\frac{\partial \mathcal{L}}{\partial \Delta\lambda} = F(\boldsymbol{\tau}_{n+1}) + s_{n+1} = 0 \quad \text{in } \Omega \tag{23}$$

$$\frac{\partial \mathcal{L}}{\partial s_{n+1}} = \mu s_{n+1}^{-1} - \Delta\lambda = 0 \Rightarrow \mu = s_{n+1}\Delta\lambda \quad \text{in } \Omega \tag{24}$$

It is apparent that the KKT conditions (19)-(22) are equivalent to the corresponding incremental equations presented in Appendix A. The last two conditions recover the yield condition and the complementarity condition shown in (50) when $\mu \to 0^+$, given that the penalty multiplier $\Delta\lambda \geq 0$, and $s_{n+1} > 0$. The essential boundary condition (40) is assumed to hold a *priori*, and thus is not reflected in the KKT conditions. From condition (22) we can also see that the newly introduced variables $\mathbf{r}$ are dynamic forces.

3.3 Material hardening/softening

The variational principle (16) can also be extended to handle more complex models involving hardening/softening yield surfaces following [34]. More specifically, the min-max program considering material hardening/softening is expressed as:

$$\begin{aligned}\min_{\Delta\mathbf{u}}\ \max_{(\boldsymbol{\sigma},\boldsymbol{\tau},\mathbf{r})_{\mathrm{n+1}}}\quad & -\frac{1}{2}\int_\Omega \Delta\boldsymbol{\sigma}^{\mathrm{T}}\mathbb{C}\Delta\boldsymbol{\sigma}\mathrm{d}\Omega+\int_\Omega \boldsymbol{\sigma}_{\mathrm{n+1}}^{\mathrm{T}}\nabla^{\mathrm{T}}(\Delta\mathbf{u})\mathrm{d}\Omega+\int_\Omega \frac{1-\theta_1}{\theta_1}\boldsymbol{\sigma}_{\mathrm{n}}^{\mathrm{T}}\nabla^{\mathrm{T}}(\Delta\mathbf{u})\mathrm{d}\Omega \\ & -\frac{1}{2}\int_\Omega \mathbf{r}_{\mathrm{n+1}}^{\mathrm{T}}\frac{\Delta t^2}{\tilde{\rho}}\mathbf{r}_{\mathrm{n+1}}\mathrm{d}\Omega+\int_\Omega \mathbf{r}_{\mathrm{n+1}}^{\mathrm{T}}\Delta\mathbf{u}\mathrm{d}\Omega \\ & -\frac{1}{2}\int_\Omega (\Delta\boldsymbol{\sigma}-\Delta\boldsymbol{\tau})^{\mathrm{T}}\frac{\theta_3\Delta t}{\eta}(\Delta\boldsymbol{\sigma}-\Delta\boldsymbol{\tau})\mathrm{d}\Omega-\int_\Omega \Delta\boldsymbol{\sigma}^{\mathrm{T}}\frac{\Delta t}{\eta}(\boldsymbol{\sigma}_{\mathrm{n}}-\boldsymbol{\tau}_{\mathrm{n}})\mathrm{d}\Omega \\ & +\int_\Omega (\boldsymbol{\sigma}_{\mathrm{n}}-\boldsymbol{\tau}_{\mathrm{n}})^{\mathrm{T}}\frac{\Delta t}{\eta}\Delta\boldsymbol{\tau}\mathrm{d}\Omega\underline{-\frac{1}{2}\int_\Omega \mathcal{H}_t^{-1}\Delta\kappa^2\mathrm{d}\Omega}-\int_\Omega \tilde{\mathbf{b}}^{\mathrm{T}}\Delta\mathbf{u}\mathrm{d}\Omega-\int_{\Gamma_{\mathrm{t}}}\tilde{\mathbf{t}}^{\mathrm{T}}\Delta\mathbf{u}\mathrm{d}\Gamma \\ \text{subject to}\quad & F(\boldsymbol{\tau}_{\mathrm{n+1}},\kappa_{\mathrm{n+1}})\le 0\end{aligned} \tag{25}$$

The underlined term is the newly introduced one with $\mathcal{H}_t$ being a new constitutive modulus associated with hardening/softening. The according KKT condition related to the variable κ is

$$\frac{\partial\mathcal{L}}{\partial\kappa_{\mathrm{n+1}}}=-\mathcal{H}_t^{-1}\Delta\kappa-\Delta\lambda\nabla_\kappa F(\boldsymbol{\tau}_{\mathrm{n+1}},\kappa_{\mathrm{n+1}})=0\Rightarrow\Delta\kappa=-\Delta\lambda\mathcal{H}_t\,\nabla_\kappa F(\boldsymbol{\tau}_{\mathrm{n+1}},\kappa_{\mathrm{n+1}}) \tag{26}$$

which is the hardening/softening law, i.e. the evolution law, for the variable κ. The constitutive modulus, $\mathcal{H}_t$, can be derived by first expanding Eq. (11) using a Taylor series

$$\kappa_{\mathrm{n+1}}=\kappa_{\mathrm{n}}+\frac{dH(\boldsymbol{\varepsilon}_{\mathrm{n}}^{\mathrm{vp}})}{d\boldsymbol{\varepsilon}^{\mathrm{vp}}}\Delta\boldsymbol{\varepsilon}^{\mathrm{vp}}\Rightarrow\Delta\kappa=\frac{dH(\boldsymbol{\varepsilon}_{\mathrm{n}}^{\mathrm{vp}})}{d\boldsymbol{\varepsilon}^{\mathrm{vp}}}\Delta\boldsymbol{\varepsilon}^{\mathrm{vp}} \tag{27}$$

Since Eq. (26) cannot be brought to be equal to the actual hardening/softening law (27) using a constant modulus, we therefore use the following tangent modulus as in [34]

$$\mathcal{H}_t=-\frac{dH(\boldsymbol{\varepsilon}_{\mathrm{n}}^{\mathrm{vp}})}{d\boldsymbol{\varepsilon}^{\mathrm{vp}}}\frac{\nabla_{\boldsymbol{\tau}}F(\boldsymbol{\tau}_{\mathrm{n}},\kappa_{\mathrm{n}})}{\nabla_\kappa F(\boldsymbol{\tau}_{\mathrm{n}},\kappa_{\mathrm{n}})} \tag{28}$$

which is updated at the beginning of each time step. Such a treatment of material hardening/softening behaviour in mathematical programming has been used successfully for approximating the hardening/softening behaviour in the Cam clay model [34].

4. Finite element formulation

The min-max program (25) can now be discretized using finite elements. For the sake of convenience, an intermediate variable $\boldsymbol{\sigma}^{\mathrm{e}} = \boldsymbol{\sigma} - \boldsymbol{\tau}$ (overstress) is introduced, which enables the optimization problem (25) to be expressed as

$$\begin{aligned}
\min_{\Delta\mathbf{u}} \max_{(\boldsymbol{\sigma},\boldsymbol{\tau},\boldsymbol{\sigma}^{\mathrm{e}},\mathbf{r})_{\mathrm{n+1}}} \quad & -\frac{1}{2}\int_\Omega \Delta\boldsymbol{\sigma}^{\mathrm{T}}\mathbb{C}\Delta\boldsymbol{\sigma}\mathrm{d}\Omega + \int_\Omega \boldsymbol{\sigma}_{\mathrm{n+1}}^{\mathrm{T}}\nabla^{\mathrm{T}}(\Delta\mathbf{u})\mathrm{d}\Omega + \int_\Omega \frac{1-\theta_1}{\theta_1}\boldsymbol{\sigma}_{\mathrm{n}}^{\mathrm{T}}\nabla^{\mathrm{T}}(\Delta\mathbf{u})\mathrm{d}\Omega \\
& -\frac{1}{2}\int_\Omega \mathbf{r}_{\mathrm{n+1}}^{\mathrm{T}}\frac{\Delta t^2}{\tilde{\rho}}\mathbf{r}_{\mathrm{n+1}}\mathrm{d}\Omega + \int_\Omega \mathbf{r}_{\mathrm{n+1}}^{\mathrm{T}}\Delta\mathbf{u}\mathrm{d}\Omega \\
& -\frac{1}{2}\int_\Omega \Delta\boldsymbol{\sigma}^{\mathrm{eT}}\frac{\theta_3\Delta t}{\eta}\Delta\boldsymbol{\sigma}^{\mathrm{e}}\mathrm{d}\Omega - \int_\Omega \Delta\boldsymbol{\sigma}^{\mathrm{eT}}\frac{\Delta t}{\eta}\boldsymbol{\sigma}_{\mathrm{n}}^{\mathrm{e}}\mathrm{d}\Omega \qquad (29) \\
& -\frac{1}{2}\int_\Omega \mathcal{H}_t^{-1}\Delta\kappa^2\mathrm{d}\Omega - \int_\Omega \tilde{\mathbf{b}}^{\mathrm{T}}\Delta\mathbf{u}\mathrm{d}\Omega - \int_{\Gamma_{\mathrm{t}}} \tilde{\mathbf{t}}^{\mathrm{T}}\Delta\mathbf{u}\mathrm{d}\Gamma \\
\text{subject to} \quad & \Delta\boldsymbol{\sigma}^{\mathrm{e}} = \Delta\boldsymbol{\sigma} - \Delta\boldsymbol{\tau} \\
& F(\boldsymbol{\tau}_{\mathrm{n+1}}, \kappa_{\mathrm{n+1}}) \le 0
\end{aligned}$$

Using standard finite element notations, we have

$$\begin{aligned}
& \boldsymbol{\sigma}(\mathbf{x}) \approx \mathbf{N}_{\boldsymbol{\sigma}}\hat{\boldsymbol{\sigma}}, \ \ \boldsymbol{\sigma}^{\mathrm{e}}(\mathbf{x}) \approx \mathbf{N}_{\boldsymbol{\sigma}^{\mathrm{e}}}\hat{\boldsymbol{\sigma}}^{\mathrm{e}}, \ \ \boldsymbol{\tau}(\mathbf{x}) \approx \mathbf{N}_{\boldsymbol{\tau}}\hat{\boldsymbol{\tau}}, \\
& \mathbf{r}(\mathbf{x}) \approx \mathbf{N}_{\mathbf{r}}\hat{\mathbf{r}}, \quad \mathbf{u}(\mathbf{x}) \approx \mathbf{N}_{\mathbf{u}}\hat{\mathbf{u}}, \qquad \nabla^{\mathrm{T}}\mathbf{u} \approx \mathbf{B}_{\mathbf{u}}\hat{\mathbf{u}}, \qquad (30) \\
& \kappa(\mathbf{x}) \approx \mathbf{N}_{\kappa}\hat{\boldsymbol{\kappa}}
\end{aligned}$$

where $\hat{\boldsymbol{\sigma}}$, $\hat{\boldsymbol{\sigma}}^{\mathrm{e}}$, $\hat{\boldsymbol{\tau}}$, $\hat{\mathbf{r}}$, $\hat{\mathbf{u}}$, and $\hat{\boldsymbol{\kappa}}$ are vectors containing the values of the corresponding field variables at interpolation points, $\mathbf{N}$ is a matrix consisting of shape functions, and $\mathbf{B}_{\mathrm{u}} = \nabla^{\mathrm{T}}\mathbf{N}_{\mathrm{u}}$. The mixed finite element shown in Figure 2 is adopted in this study, where the distribution of the interpolation points for the different variables is depicted. Substituting the above equations into the program (29) leads to

$$\begin{aligned}\min_{\Delta\hat{\mathbf{u}}}\ \max_{(\hat{\boldsymbol{\sigma}},\hat{\boldsymbol{\tau}},\hat{\boldsymbol{\sigma}}^{\mathrm{e}},\hat{\mathbf{r}},\hat{\boldsymbol{\kappa}})_{\mathrm{n+1}}}\quad & -\frac{1}{2}\Delta\hat{\boldsymbol{\sigma}}^{\mathrm{T}}\mathbf{C}\Delta\hat{\boldsymbol{\sigma}}+\Delta\hat{\mathbf{u}}^{\mathrm{T}}\mathbf{B}^{\mathrm{T}}\hat{\boldsymbol{\sigma}}_{\mathrm{n+1}}+\Delta\hat{\mathbf{u}}^{\mathrm{T}}\frac{1-\theta_1}{\theta_1}\mathbf{B}^{\mathrm{T}}\hat{\boldsymbol{\sigma}}_{\mathrm{n}}\\ & -\frac{1}{2}\hat{\mathbf{r}}_{\mathrm{n+1}}^{\mathrm{T}}\mathbf{D}\hat{\mathbf{r}}_{\mathrm{n+1}}+\Delta\hat{\mathbf{u}}^{\mathrm{T}}\mathbf{A}^{\mathrm{T}}\hat{\mathbf{r}}_{\mathrm{n+1}}-\frac{1}{2}\Delta\hat{\boldsymbol{\sigma}}^{\mathrm{eT}}\mathbf{M}\Delta\hat{\boldsymbol{\sigma}}^{\mathrm{e}}\\ & -\Delta\hat{\boldsymbol{\sigma}}^{\mathrm{eT}}\mathbf{f}^{\mathrm{c}}-\frac{1}{2}\Delta\hat{\boldsymbol{\kappa}}^{\mathrm{T}}\mathbf{H}\Delta\hat{\boldsymbol{\kappa}}-\Delta\hat{\mathbf{u}}^{\mathrm{T}}\mathbf{f}^{\mathrm{e}}\\ \text{subject to}\quad & \Delta\hat{\boldsymbol{\sigma}}^{\mathrm{e}}=\Delta\hat{\boldsymbol{\sigma}}-\Delta\hat{\boldsymbol{\tau}}\\ & F_j\,(\hat{\boldsymbol{\tau}}_{\mathrm{n+1}},\hat{\boldsymbol{\kappa}}_{\mathrm{n+1}})\le 0,\quad j=1,2,\cdots,N_G\end{aligned}\tag{31}$$

where

$$\begin{aligned}&\mathbf{C}=\int_\Omega \mathbf{N}_{\boldsymbol{\sigma}}^{\mathrm{T}}\mathbb{C}\mathbf{N}_{\boldsymbol{\sigma}}\mathrm{d}\Omega,\quad \mathbf{B}^{\mathrm{T}}=\int_\Omega \mathbf{B}_{\mathbf{u}}^{\mathrm{T}}\mathbf{N}_{\boldsymbol{\sigma}}\mathrm{d}\Omega,\\ &\mathbf{D}=\int_\Omega \mathbf{N}_{\mathbf{r}}^{\mathrm{T}}\frac{\Delta t^2}{\tilde{\rho}}\mathbf{N}_{\mathbf{r}}\mathrm{d}\Omega,\quad \mathbf{A}^{\mathrm{T}}=\int_\Omega \mathbf{N}_{\mathbf{u}}^{\mathrm{T}}\mathbf{N}_{\mathbf{r}}\mathrm{d}\Omega,\\ &\mathbf{M}=\int_\Omega \mathbf{N}_{\boldsymbol{\sigma}^{\mathrm{e}}}^{\mathrm{T}}\frac{\theta_3\Delta t}{\eta}\mathbf{N}_{\boldsymbol{\sigma}^{\mathrm{e}}}\mathrm{d}\Omega,\quad \mathbf{H}=\int_\Omega \mathbf{N}_{\kappa}^{\mathrm{T}}\frac{1}{\mathcal{H}_t}\mathbf{N}_{\kappa}\mathrm{d}\Omega,\\ &\mathbf{f}^{\mathrm{e}}=\int_\Omega \mathbf{N}_{\mathbf{u}}^{\mathrm{T}}\tilde{\mathbf{b}}\mathrm{d}\Omega+\int_{\Gamma_{\mathrm{t}}}\mathbf{N}_{\mathbf{u}}^{\mathrm{T}}\tilde{\mathbf{t}}\mathrm{d}\Gamma,\ \mathbf{f}^{\mathrm{c}}=\int_\Omega \mathbf{N}_{\boldsymbol{\sigma}}^{\mathrm{T}}\frac{\Delta t}{\eta}\boldsymbol{\sigma}_{\mathrm{n}}^{\mathrm{e}}\mathrm{d}\Omega\end{aligned}\tag{32}$$

The yield conditions are enforced at all Gauss integration points, with N_G being the total number of such points. After solving the minimization part over Δu of program (31), and transforming the maximum into a minimum with an opposite sign, we obtain

$$\begin{aligned}\min_{(\hat{\boldsymbol{\sigma}},\hat{\boldsymbol{\tau}},\hat{\boldsymbol{\sigma}}^{\mathrm{e}},\hat{\mathbf{r}},\hat{\boldsymbol{\kappa}})_{\mathrm{n+1}}}\quad & \frac{1}{2}\Delta\hat{\boldsymbol{\sigma}}^{\mathrm{T}}\mathbf{C}\Delta\hat{\boldsymbol{\sigma}}+\frac{1}{2}\hat{\mathbf{r}}_{\mathrm{n+1}}^{\mathrm{T}}\mathbf{D}\hat{\mathbf{r}}_{\mathrm{n+1}}+\frac{1}{2}\Delta\hat{\boldsymbol{\sigma}}^{\mathrm{eT}}\mathbf{M}\Delta\hat{\boldsymbol{\sigma}}^{\mathrm{e}}\\ & +\frac{1}{2}\Delta\hat{\boldsymbol{\kappa}}^{\mathrm{T}}\mathbf{H}\Delta\hat{\boldsymbol{\kappa}}+\Delta\hat{\boldsymbol{\sigma}}^{\mathrm{eT}}\mathbf{f}^{\mathrm{c}}\\ \text{subject to}\quad & \mathbf{B}^{\mathrm{T}}\hat{\boldsymbol{\sigma}}_{\mathrm{n+1}}+\frac{1-\theta_1}{\theta_1}\mathbf{B}^{\mathrm{T}}\hat{\boldsymbol{\sigma}}_{\mathrm{n}}+\mathbf{A}^{\mathrm{T}}\hat{\mathbf{r}}_{\mathrm{n+1}}-\mathbf{f}^{\mathrm{e}}=\mathbf{0}\\ & \Delta\hat{\boldsymbol{\sigma}}^{\mathrm{e}}=\Delta\hat{\boldsymbol{\sigma}}-\Delta\hat{\boldsymbol{\tau}}\\ & F_j\,(\hat{\boldsymbol{\tau}}_{\mathrm{n+1}},\hat{\boldsymbol{\kappa}}_{\mathrm{n+1}})\le 0,\quad j=1,2,\cdots,N_G\end{aligned}\tag{33}$$

The natural boundary condition (44) has been included through the terms $\mathbf{f}^{\mathrm{e}}$, whereas the imposition of essential boundary conditions for the displacements requires the introduction of a new variable $\hat{\mathbf{r}}_{\mathrm{n+1}}^{\mathrm{u}}$ since the displacement increment $\Delta\mathbf{u}$ is a field variable for the dual problem of program (33). More specifically, the program turns out to be

$$
\begin{aligned}
\min_{(\hat{\boldsymbol{\sigma}},\hat{\boldsymbol{\tau}},\hat{\boldsymbol{\sigma}}^{\mathrm{e}},\hat{\mathbf{r}},\hat{\boldsymbol{\kappa}},\hat{\mathbf{r}}^{\mathrm{u}})_{\mathrm{n+1}}} \quad & \frac{1}{2}\Delta\hat{\boldsymbol{\sigma}}^{\mathrm{T}}\mathbf{C}\Delta\hat{\boldsymbol{\sigma}} + \frac{1}{2}\hat{\mathbf{r}}_{\mathrm{n+1}}^{\mathrm{T}}\mathbf{D}\hat{\mathbf{r}}_{\mathrm{n+1}} + \frac{1}{2}\Delta\hat{\boldsymbol{\sigma}}^{\mathrm{eT}}\mathbf{M}\Delta\hat{\boldsymbol{\sigma}}^{\mathrm{e}} \\
& + \frac{1}{2}\Delta\hat{\boldsymbol{\kappa}}^{\mathrm{T}}\mathbf{H}\Delta\hat{\boldsymbol{\kappa}} + \Delta\hat{\boldsymbol{\sigma}}^{\mathrm{eT}}\mathbf{f}^{\mathrm{c}} - \underline{(\mathbf{E}\mathbf{U}^{\mathrm{d}})^{\mathrm{T}}\hat{\mathbf{r}}_{\mathrm{n+1}}^{\mathrm{u}}} \\
\text{subject to} \quad & \mathbf{B}^{\mathrm{T}}\hat{\boldsymbol{\sigma}}_{\mathrm{n+1}} + \mathbf{A}^{\mathrm{T}}\hat{\mathbf{r}}_{\mathrm{n+1}} - \underline{\mathbf{E}\hat{\mathbf{r}}_{\mathrm{n+1}}^{\mathrm{u}}} = \mathbf{f}^{\mathrm{e}} - \frac{1-\theta_1}{\theta_1}\mathbf{B}^{\mathrm{T}}\hat{\boldsymbol{\sigma}}_{\mathrm{n}} \\
& \Delta\hat{\boldsymbol{\sigma}}^{\mathrm{e}} = \Delta\hat{\boldsymbol{\sigma}} - \Delta\hat{\boldsymbol{\tau}} \\
& F_j\,(\hat{\boldsymbol{\tau}}_{\mathrm{n+1}},\hat{\boldsymbol{\kappa}}_{\mathrm{n+1}}) \le 0, \quad j = 1, 2, \cdots, N_G
\end{aligned}
\tag{34}
$$

where the essential boundary condition (44) are enforced, $\mathbf{E}$ is an index matrix consisting of entries equal to 0 and 1, $\mathbf{U}^{\mathrm{d}}$ is a vector consisting of the prescribed displacements at mesh nodes, and the newly introduced $\hat{\mathbf{r}}_{\mathrm{n+1}}^{\mathrm{u}}$ represents the nodal reaction force. As shown, both the objective function and the constraints of program (34) are altered (the underlined terms) due to the imposition of the essential boundary conditions. The validity of the above can be checked by differentiating the Lagrangian associated with the program (34) with respect to $\hat{\mathbf{r}}_{\mathrm{n+1}}^{\mathrm{u}}$, resulting in

$$
\frac{\partial \mathcal{L}}{\partial \hat{\mathbf{r}}_{\mathrm{n+1}}^{\mathrm{u}}} = \mathbf{E}\mathbf{U}^{\mathrm{d}} - \mathbf{E}\Delta\hat{\mathbf{u}}_{\mathrm{n+1}} = \mathbf{0}
\tag{35}
$$

This is obviously the discretised form of the displacement boundary conditions (45).

Interaction between a deformable body and a rigid surface can be achieved in a straightforward manner in the above program according to [35]. The classical Coulomb model for frictional contact is adopted in this study, which is

$$
\begin{aligned}
& g_N \ge 0, \quad p \ge 0, \quad p g_N = 0, \\
& |q| - \mu p \le 0
\end{aligned}
\tag{36}
$$

As shown in Figure 3, g_N is the gap between the material and the rigid surface, p is the contact pressure which is positive corresponding to compression, q is the tangential stress, and μ is the friction coefficient between the material and the surface. After enforcing the conditions in (36) on finite element nodes, the principle reads

$$
\begin{aligned}
\min_{(\hat{\boldsymbol{\sigma}},\hat{\boldsymbol{\tau}},\hat{\boldsymbol{\sigma}}^{\mathrm{e}},\hat{\mathbf{r}},\hat{\boldsymbol{\kappa}},\hat{\mathbf{r}}^{\mathrm{u}})_{\mathrm{n+1}}} \quad & \frac{1}{2}\Delta\hat{\boldsymbol{\sigma}}^{\mathrm{T}}\mathbf{C}\Delta\hat{\boldsymbol{\sigma}} + \frac{1}{2}\hat{\mathbf{r}}_{\mathrm{n+1}}^{\mathrm{T}}\mathbf{D}\hat{\mathbf{r}}_{\mathrm{n+1}} + \frac{1}{2}\Delta\hat{\boldsymbol{\sigma}}^{\mathrm{eT}}\mathbf{M}\Delta\hat{\boldsymbol{\sigma}}^{\mathrm{e}} \\
& + \frac{1}{2}\Delta\hat{\boldsymbol{\kappa}}^{\mathrm{T}}\mathbf{H}\Delta\hat{\boldsymbol{\kappa}} + \Delta\hat{\boldsymbol{\sigma}}^{\mathrm{eT}}\mathbf{f}^{\mathrm{c}} - (\mathbf{E}\mathbf{U}^{\mathrm{d}})^{\mathrm{T}}\hat{\mathbf{r}}_{\mathrm{n+1}}^{\mathrm{u}} + \sum_{j=1}^{n_c} g_{0j} p_j \\
\text{subject to} \quad & \mathbf{B}^{\mathrm{T}}\hat{\boldsymbol{\sigma}}_{\mathrm{n+1}} + \mathbf{A}^{\mathrm{T}}\hat{\mathbf{r}}_{\mathrm{n+1}} - \mathbf{E}\hat{\mathbf{r}}_{\mathrm{n+1}}^{\mathrm{u}} + \mathbf{E}^{\mathrm{c}}\boldsymbol{\rho} = \mathbf{f}^{\mathrm{e}} - \frac{1-\theta_1}{\theta_1}\mathbf{B}^{\mathrm{T}}\hat{\boldsymbol{\sigma}}_{\mathrm{n}} \\
& \Delta\hat{\boldsymbol{\sigma}}^{\mathrm{e}} = \Delta\hat{\boldsymbol{\sigma}} - \Delta\hat{\boldsymbol{\tau}} \\
& p_k = -\mathbf{n}^{\mathrm{T}}\boldsymbol{\rho}_k, \quad k = 1,\ldots,n_c \\
& q_k = -\hat{\mathbf{n}}^{\mathrm{T}}\boldsymbol{\rho}_k, \quad |q_k| - \mu p_k \le 0 \\
& F_j^*(\hat{\boldsymbol{\tau}}_{\mathrm{n+1}}, \hat{\boldsymbol{\kappa}}_{\mathrm{n+1}}) \le 0, \quad j = 1, 2, \cdots, N_G
\end{aligned}
\tag{37}
$$

where $\boldsymbol{\rho} = (\rho_1, \rho_2)^{\mathrm{T}}$ are the nodal forces, $\mathbf{n} = (n_1, n_2)^{\mathrm{T}}$ and $\hat{\mathbf{n}} = (-n_2, n_1)^{\mathrm{T}}$ are the normal and the tangent to the rigid boundary, $\mathbf{E}^{\mathrm{c}}$ is an index matrix of zeros and ones, and n_c is the number of potential contacts. The above program is the final optimization problem to be solved. While it may be solved in a number of ways using either general or specialized methods, it is transformed here into a second-order cone program (SOCP) and then resolved using the high performance optimization solver MOSEK [4]. The transformation of programs of the same type as (37) into a SOCP is straightforward, and has been documented in detail in [23, 34]. The main operation is to recast the quadratic terms in the objective function to linear ones, subject to a quadratic constraint, and to reform the yield function as a cone. Due to the attractive advantages presented in the introduction, a variety of mechanics problems have been formulated and solved in such a manner, including computational limit analysis of solids and plates [36-38], static/dynamic analysis of elastoplastic frames and solids [21, 35, 39, 40], analysis of steady-state non-Newtonian fluid flows [41], consolidation analysis [23], and the analysis of granular contact dynamics [42-44].

5. Particle Finite Element Method

The Particle Finite Element Method (PFEM) is a Lagrangian approach capable of handling general large deformation problems without any real limitation on the magnitude of the deformation [27, 29, 45, 46]. Its major characteristic is to treat mesh nodes as ‘particles’ that can move freely, and even separate from, the computational domain to which they originally belong. The basic steps of the utilized PFEM are summarized (see also Figure 4) in the following, with more details given in [35]:

(1) Suppose that we have a cloud of particles, C^{n}, at time t_{n} ;

(2) Identify the computational domain using the α-shape method [47] on the basis of C^{n};

(3) Create a finite element mesh, M^{n}, through a triangulation of the recognized domain and discretize governing equations on M^{n};

(4) Map the state variables such as stresses, strains, velocities, etc. from the old mesh, $M^{\mathrm{n-1}}$, to the new mesh, M^{n};

(5) Solve the discrete governing equations on the new mesh, M^{n}, through a standard finite element procedure;

(6) Update the position of mesh nodes to arrive at $C^{\mathrm{n+1}}$ and repeat.

To date, a number of challenging problems involving large deformation and free-surface evolution have been tackled by the PFEM. These include the modelling of granular flows [24, 25, 35, 48, 49], landslides [29, 50], landslide-generated waves [30, 46], multi-fluid flows [51-53], fluid-structure interaction [27, 54, 55], soil-structure interaction [35, 40], bubble dynamics [56], the melting and spreading of polymers [57], industrial forming processes, and the flow of fresh cement [58]. In this paper, the solution algorithm for elastoviscoplastic analysis with strain softening is incorporated into the PFEM for progressive failure analysis of sensitive clays. It is notable that the governing equations proposed are on the basis of the infinitesimal strain theory which may lead to several errors for large deformation analysis. The most serious one is the generation of strains as a result of rigid body motion. However, it has been shown in [35, 59] that this and related errors are relatively minor when the time steps used are small. As such, the price to pay for the convenience of being able to operate with usual infinitesimal strain theory appears to be very small. Indeed, such a strategy has been verified against analytical solutions for penetration problems [60] and validated qualitatively as well as quantitatively against both quasi-static and dynamic collapse of a granular column [24, 25] and the penetration of shallowly embedded pipelines [61]. Furthermore, it succeeds in reproducing a real-world flow-like landslide [29].

6. Numerical Examples

This section discusses numerical results for progressive failure analysis of sensitive clays using the proposed approach. Note that finite element analysis of strain-softening materials encounters issues of mesh sensitivity when using rate-independent models because the field equations that describe the motion of the body may lose hyperbolicity. Indeed, the corresponding boundary-value problem becomes ill-posed, with pathologically mesh-dependent solutions in which the width of the shear bands depends on the mesh size. The application of rate-dependent models is an effective way to circumvent this problem. It has been shown that viscous terms introduce a length scale effect into the initial boundary-value problem, even the rate-dependent model does not explicitly contain a parameter with the dimension of length [62, 63]. Consequently, viscoplastic models result in solutions where the shear bands have a finite width when strain localization occurs. It should be noted, however, that the main objective of this work is to capture the entire failure process in sensitive clays involving large deformation, rather than to predict the thickness of localized shear bands. As noted by Moore [64], the typical thickness of a shear band in clay at failure is between 0.01 and 2 cm, and thus it is impractical to predict both the microscopic and macroscopic soil response using a purely continuum model where a large earth structure is considered. One possible way of accounting for the responses on both the macro and micro levels is through the multiscale computational modelling technique [65-68].

6.1 One-dimensional elasto-viscoplastic problem

To verify the proposed variational principle, we consider an axial bar subject to a prescribed load (Figure 5(a)). The material is represented by a one-dimensional elastoviscoplastic model (Figure 5(b)). If the mass of the bar is sufficiently small, so that any induced inertial forces are negligible, the load produces a uniform stress and strain along the bar and an analytical solution is available. In the following, the material parameters of the bar are assumed to be: Young's modulus $E = 5\times10^4$ Pa, the initial yield stress $\sigma_{Y_0} = 100$ Pa, and the viscosity coefficient $\eta = 1000$ $\mathrm{Pa}\cdot\mathrm{s}$.

The ability of the proposed formulation to capture the strain-rate dependence of the stress response and stress relaxation behaviour is examined first. To this end, we set the prescribed strain increase at a constant rate α until time $t^* = 0.4$ s and then hold the strain constant, leading to stress relaxation. The analytical solution of this problem is available [69] and we consider three different load rates, namely α =0.2, 0.4, and 0.6, respectively, to produce a rate-dependent response (Figure 6(a)). The yield stress is set to be constant ($\sigma_Y = \sigma_{Y_0}$) in this case (Figure 6(b)) and the time increment is $\Delta t = 2\times10^{-3}$ s in all simulations. Figure 7 illustrates the simulated stress response for different load rates as well as the corresponding analytical solutions. For all cases, the resulting stresses increase in a stable manner until their maximum values are reached. A higher load rate results in a larger maximum stress reflecting the effect of viscosity. At the time $t = t*$, the stresses for all three cases drop sharply representing stress relaxation behaviour. Eventually, the residual stresses for all cases asymptote towards the initial stress strength of the material, σ_{Y_0}. All the simulated results agree with the analytical solutions, which verifies the proposed variational formulation and finite element implementation.

We now consider the details of strain-softening behaviour. The prescribed strain in this case increases with a constant rate α =0.2 (Figure 8(a)); however the yield stress strength σ_Y, which equals $\sigma_{Y_0} = 100\,\mathrm{Pa}$ at the beginning, reduces to its residual value $\sigma_{YR} = 30\%\sigma_{Y_0}$ when the accumulated plastic strain reaches 7% (Figure 8(b)). Such a phenomenon of reduction has been widely observed for materials undergoing plastic deformation. The initial and residual yield stress strengths can be interpreted as strengths of a material at undisturbed and remoulded states. The simulation is conducted using a total of 20, 30, and 40 time increments, respectively, and again the agreement between the numerical and analytical solutions is satisfactory (Figure 9).

6.2 Collapse of a sensitive clay column

As the second example, we consider the collapse of a sensitive clay column (Figure 10) in a container which is 50 cm wide and 100 cm high. The container is lifted up quickly leading to the spread of the sensitive clay. Such an experimental test has been widely used for investigating the behaviour of granular matter [70-74], but has also been adopted for studying the quickness of sensitive clays [1]. Here, the problem is considered to deform under plane-strain conditions and only half of the geometry is modelled due to the symmetry. The material parameters are as follows: Young's modulus $E = 5\times10^6$ Pa, Poisson's ratio $\upsilon = 0.49$, density $\rho = 1.8\times10^3$ kg/m^3, viscosity coefficient $\eta = 100\ \text{Pa}\cdot\text{s}$, undisturbed shear strength $c_{\text{up}} = 5$ kPa, remoulded shear strength $c_{\text{ur}} = 1$ kPa, and $\bar{\kappa} = 25\%$. The frictional coefficient between the clay and the rigid surface is taken as 0.3 and the gravitational acceleration $g = -9.8$ m/s^2. The column is discretized using 7,962 6-node triangular elements with 16,199 nodes, and the time step utilized is $\Delta t = 0.01$ s.

The collapse procedure of the column obtained from the simulation is illustrated in Figure 11, in which the colour is proportional to the accumulated equivalent plastic strain. The normalized time $\bar{t}$ refers to $\frac{t}{\sqrt{2h_0/\text{g}}}$ with h_0 being the initial height of the column. For initially undisturbed sensitive clays, lifting the container results in two shear bands dividing the column into three parts (Figure 11(a)). The upper part moves downward while the middle part, which is in the shape of a triangle, is pushed out horizontally. After a considerable movement of the middle part, a shear band is formed in the lower part (Figure 11(b)) and then one more shear band appears in the upper part (Figure 11(c)). The second shear band in the upper part deforms another layer of sensitive clay and the lower part, which was intact, is disturbed significantly because of the shear band formed (Figure 11(d)). Further collapse of the column leads to two more layers being squeezed out (Figure 11(e) and (f)). Localized shear bands can be observed clearly in the final deposit, with some parts of the column remaining undisturbed throughout the failure process. The collapse of remoulded sensitive clay is also simulated for comparison (Figure 11). As shown, the collapse mechanism for this case is quite different to the previous case of an undisturbed sample. Rather than fail progressively, nearly all the material experiences plastic deformation with the material near the bottom possessing the maximum equivalent plastic strain. Figure 12 shows the curves of the front location and centre height against normalized time for columns of both initially undisturbed and remoulded sensitive clays. The collapse of the column of remoulded clay results in a final deposit with a much smaller height and considerably larger length. Both the sensitive and remoulded clay columns reach their maximum run-out distance at around $\bar{t}=2.15$. However, the final centre height for the remoulded case is obtained earlier ($\bar{t}=1.4$) than that for the initially undisturbed case ($\bar{t}=2.15$). Notably, the final centre height and length are obtained simultaneously for the undisturbed sample, which differs from that for the remoulded sample. The final mesh topology for both cases, illustrated in Figure 13, verifies that the proposed approach can handle the extreme mesh distortion that accompanies failure for this problem. A video of the collapse of both the remoulded and undisturbed sensitive clay columns is provided in the supplementary materials.

To estimate the mesh sensitivity, the collapse of the initially undisturbed clay was also re-analyzed using three different mesh sizes, where the length of the element edge was set to $h=1.0$ cm (1,934 triangles), 0.75 cm (3,528 triangles) and 0.5 cm (7,962 triangles). The cases are referred to as coarse, medium, and fine meshes. As shown in Figure 14, the curves of locations against time for all three tests agree well with each other. Moreover, all three simulations result in very similar final deposits and shear bands (Figure 15), which proves that a further decrease in the mesh size will not alter the form of the predicted failure mode.

6.3 Retrogressive collapse of a slope in sensitive clay

As observed in Scandinavia and eastern Canada, a fast and significant retrogressive collapse of a slope in sensitive clay may be triggered by a small initial slide [2]. To illustrate the ability of the proposed approach for modelling such a geohazard, we consider the sensitive clay deposit shown in Figure 16. Here, collapse is triggered by removing a rigid triangular block at the toe of the slope (which may be caused by erosion or excavation). The material parameters of the sensitive clay are as follows: Young's modulus $E = 5 \times 10^6$ Pa, Poisson's ratio $\upsilon = 0.33$, density $\rho = 1.8 \times 10^3$ kg/m^3, viscosity coefficient $\eta = 100$ Pa$\cdot$s, undisturbed shear strength $c_{\mathrm{uu}} = 22$ kPa, remoulded shear strength $c_{\mathrm{ur}} = 1.2$ kPa, and $\bar{\kappa} = 25\%$. The frictional coefficient between the sensitive clay and the rigid bottom surface is set to 0.1 and the gravitational acceleration $g = -9.8$ m/s^2. A total of 18,420 6-noded triangular elements (37,355 mesh nodes) is used to discretize the initial computational domain. The time step is $\Delta t = 0.025$ s and the simulation proceeds until the final deposit is obtained.

The retrogressive failure process from the simulation is illustrated in Figure 17, with the colour being proportional to the accumulated equivalent plastic strain. As illustrated, the erosion leads to the first retrogressive collapse C1 in the slope (Figure 17(b)). Two shear bands initiate from the bottom and propagate towards the top surface and the front inclined surface, respectively, resulting in a graben. During the sliding, one more shear band is generated in the graben dividing it into two elastic parts (Figure 17(c) and (d)). As the disturbed mass due to collapse C1 moves far away from the new slip surface, the second retrogressive collapse C2 occurs (Figure 17(e) and (f)). This mimics the first criterion for the occurrence of retrogressive failure, that the slide debris should be able to flow out of the slide area [1]. The same as that in C1, two plastic shear bands, also originating from the slope base, are formed in C2 which results in a graben and a horst. The mass in front of the new slope surface continues to move forward leading to the third retrogressive failure of the slope, C3 (Figure 17(g)). After this, a considerable amount of mass is deposited in front of the new slope surface, resisting further collapse (Figure 17(h)). The final configuration of the slope, shown in Figure 17(i), indicates that most of the clay involved in C2 and C3 has been remoulded. This reflects the other criterion for the occurrence of retrogressive failure, which states that the slide debris should be completely remoulded [1]. Eventually, the retrogressive failure results in a deposit with a run-out distance of 28.71 m and a retrogression distance of 14.76 m (Figure 17(i)). A video of the entire failure process of the slope is available in the supplementary materials.

The velocity of the sliding front and the maximum velocity were also recorded and are depicted in Figure 18. As illustrated, the maximum velocity is not always located at the sliding front. This can be explained by examining the velocity contour (Figure 19). The first retrogressive failure results in the transformation of a part of the gravitational potential energy of the mass into kinetic energy, with the remaining energy being dissipated by plastic shearing (Figure 19(a)). The sliding front thus possesses the maximum velocity due to this transformation. The second retrogressive collapse further releases potential gravitational energy (Figure 19(b) and pushes the materials in front of it, consequently increasing the velocity of the corresponding mass. In contrast, the velocity of the sliding front decreases because of the friction along the basal surface and the effects of plastic dissipation. After a while, the mass at the middle moves faster than the sliding front does as shown in Figure 19(c). The third retrogressive collapse further releases potential gravitational energy (Figure 19(d)). The velocity of the involved mass in collapse C3 is relatively low, however, because a considerable body of clay with low velocity is located in front of the new slope surface. Note that the sliding front already ceased at $t = 11.4$ s (Figure 19(e)). However, the clay at the middle of the sliding mass continues to be pushed and moves forward, which eventually disturbs the sliding front (Figure 19(f) and (g)).

The value of viscosity, back-calculated from various subaerial and submarine slides by Edgers and Karlsrud [75] and Johnson and Rodine [76], is in the range of 100 to 1499 $\mathrm{Pa \cdot s}$. We here investigate the effect of the viscosity on the retrogressive failure by analysing the problem with varying viscosity coefficients of $\eta = 1\ \mathrm{Pa \cdot s}$, 10 $\mathrm{Pa \cdot s}$, 100 $\mathrm{Pa \cdot s}$, and 1000 $\mathrm{Pa \cdot s}$. Other material parameters for these simulations are the same as in the previous case. As shown in Figure 20, retrogressive failure occurs four times for both $\eta = 1\ \mathrm{Pa \cdot s}$ and 10 $\mathrm{Pa \cdot s}$. Thus, the retrogression distances for these two cases, 20.25 m and 20.13 m, are very close (Figure 21), although the run-out distance for $\eta = 1\ \mathrm{Pa \cdot s}$ (38.18 m) is slightly larger than that for $\eta = 10\ \mathrm{Pa \cdot s}$ (36.73 m). When η is increased further, fewer retrogressive failures are induced: for example three times for $\eta = 100\ \mathrm{Pa \cdot s}$ and only twice for $\eta = 1000\ \mathrm{Pa \cdot s}$ (Figure 20). This means that an increase of η ($\eta > 10\ \mathrm{Pa \cdot s}$) causes a decrease in the run-out and retrogressive distance, as illustrated in Figure 21, because a higher viscosity results in much more plastic dissipation and, consequently, less potential gravitational energy is converted into kinetic energy. Such a decrease in energy transformation not only leads to a smaller run-out distance, but also causes more clay to be deposited in front of the newly formed slope surface which resists the occurrence of further retrogressive failure.

7. Conclusions

The progressive failure process of sensitive clays is simulated using the Particle Finite Element Method with an advanced elastoviscoplastic model which is a combination of the Bingham model (for describing rheological behaviour) and the Tresca model with strain-softening (for capturing progressive failure behaviour). The resulting elastoviscoplastic analysis is reformulated as an optimization problem on the basis of a mixed variational principle and resolved in mathematical programming.

The proposed formulation is verified against the analytical solution of a one-dimensional elastoviscoplastic problem. The capability of the proposed computational approach for modelling progressive failure is illustrated by simulating the collapse of a column of sensitive clay. Additionally, the retrogressive failure of a slope in sensitive clay is reproduced successfully. The simulation results reflect the essential conditions for the occurrence of retrogressive collapse which are that the slide debris should be fully remoulded and flow away from the slide area. Furthermore, the effect of the viscosity of a sensitive clay on the nature of retrogressive collapse is also studied. Numerical results show that an increase of viscosity leads to a decrease in both the run-out distance and the retrogression distance due to the dissipation of a large amount of energy.

Although the problem in this study is simulated under undrained conditions using total stresses, an effective stress analysis can also be performed. This can be achieved by merging the SOCP formulation for consolidation analysis of saturated porous media introduced in [23], where rate-independent models are utilised, with the mixed variational principle presented in this paper. The resulting formulation then can be incorporated into the particle finite element method for investigating the hydro-mechanical mechanism in the progressive failure of sensitive clays.

Acknowledgements The authors wish to acknowledge the support of the Australian Research Council Centre of Excellence for Geotechnical Science and Engineering and the Australian Research Council Discovery Project funding scheme (Project Number DP150104257).

Appendix A. Time discretization

The momentum conservation equation (1) is first discretized in time using the standard θ-method as:

$$\nabla^{\mathrm{T}}[\theta_1\boldsymbol{\sigma}_{\mathrm{n+1}} + (1-\theta_1)\boldsymbol{\sigma}_{\mathrm{n}}] + \mathbf{b} = \rho\frac{\mathbf{v}_{\mathrm{n+1}} - \mathbf{v}_{\mathrm{n}}}{\Delta t} \tag{38}$$

$$\theta_2\mathbf{v}_{\mathrm{n+1}} + (1-\theta_2)\mathbf{v}_{\mathrm{n}} = \frac{\mathbf{u}_{\mathrm{n+1}} - \mathbf{u}_{\mathrm{n}}}{\Delta t} \tag{39}$$

where $\mathbf{v}$ are velocities, θ_1 and θ_2 are parameters taking values in [0, 1], the subscripts n and n+1 refer to the known and new, unknown states, and $\Delta t = t_{\mathrm{n+1}} - t_{\mathrm{n}}$ is the time step. Rearranging the above equations leads to

$$\nabla^{\mathrm{T}}\boldsymbol{\sigma}_{\mathrm{n+1}} + \frac{1-\theta_1}{\theta_1}\nabla^{\mathrm{T}}\boldsymbol{\sigma}_{\mathrm{n}} + \tilde{\mathbf{b}} = \tilde{\rho}\frac{\Delta\mathbf{u}}{\Delta t^2} \tag{40}$$

$$\mathbf{v}_{\mathrm{n+1}} = \frac{1}{\theta_2}\left[\frac{\Delta\mathbf{u}}{\Delta t} - (1-\theta_2)\mathbf{v}_{\mathrm{n}}\right] \tag{41}$$

with the displacement increments $\Delta\mathbf{u} = \mathbf{u}_{\mathrm{n+1}} - \mathbf{u}_{\mathrm{n}}$ and

$$\tilde{\rho} = \frac{\rho}{\theta_1\theta_2} \tag{42}$$

$$\tilde{\mathbf{b}} = \frac{1}{\theta_1}\mathbf{b} + \tilde{\rho}\frac{\mathbf{v}_{\mathrm{n}}}{\Delta t} \tag{43}$$

The natural boundary condition is approximated in an analogous manner leading to

$$\mathbf{N}^{\mathrm{T}}(\boldsymbol{\sigma}_{\mathrm{n+1}} + \frac{1-\theta_1}{\theta_1}\boldsymbol{\sigma}_{\mathrm{n}}) = \tilde{\mathbf{t}} \quad \text{on } \Gamma_{\mathrm{t}} \quad \text{with } \tilde{\mathbf{t}} = \frac{1}{\theta_1}\bar{\mathbf{t}} \tag{44}$$

and the discretised essential boundary condition is

$$\mathbf{u}_{\mathrm{n+1}} = \bar{\mathbf{u}}_{\mathrm{n+1}} \quad \text{on } \Gamma_{\mathrm{u}} \tag{45}$$

By introducing another parameter $\theta_3 \in [0,\ 1]$, the incremental equations of the elastoviscoplastic model (Eqs. (6)-(10)) are

$$\Delta\boldsymbol{\varepsilon} = \Delta\boldsymbol{\varepsilon}^{\mathrm{e}} + \Delta\boldsymbol{\varepsilon}^{\mathrm{vp}} \tag{46}$$

$$\Delta\boldsymbol{\varepsilon}^{\mathrm{e}} = \mathbb{C}\Delta\boldsymbol{\sigma} \tag{47}$$

$$(\boldsymbol{\sigma}_{\mathrm{n}} + \theta_3\Delta\boldsymbol{\sigma}) - (\boldsymbol{\tau}_{\mathrm{n}} + \theta_3\Delta\boldsymbol{\tau}) = \eta\frac{\Delta\boldsymbol{\varepsilon}^{\mathrm{vp}}}{\Delta t} \quad \Rightarrow \quad (\Delta\boldsymbol{\sigma} - \Delta\boldsymbol{\tau}) + \frac{1}{\theta_3}(\boldsymbol{\sigma}_{\mathrm{n}} - \boldsymbol{\tau}_{\mathrm{n}}) = \frac{\eta}{\theta_3\Delta t}\Delta\boldsymbol{\varepsilon}^{\mathrm{vp}} \tag{48}$$

$$\Delta\boldsymbol{\varepsilon}^{\mathrm{vp}} = \Delta\lambda\nabla_G F(\boldsymbol{\tau}_{\mathrm{n+1}}) \tag{49}$$

$$F(\boldsymbol{\tau}_{\mathrm{n+1}}) \le 0; \Delta\lambda \ge 0; \Delta\lambda F(\boldsymbol{\tau}_{\mathrm{n+1}}) = 0 \tag{50}$$

In summary, the governing equations for incremental analysis of elastoviscoplasticity consist of Eqs. (40), (41), (44)-(50).

Reference

1. Thakur, V. and Degago, S.A., Quickness of sensitive clays. *Géotechnique Letters*, 2012. **2**(3): p. 87-95.
2. Locat, A., Leroueil, S., Bernander, S., Demers, D., Jostad, H.P., and Ouehb, L., Progressive failures in eastern Canadian and Scandinavian sensitive clays. *Canadian Geotechnical Journal*, 2011. **48**(11): p. 1696-1712.
3. Jeong, S.W., Determining the viscosity and yield surface of marine sediments using modified Bingham models. *Geosciences Journal*, 2013. **17**(3): p. 241-247.
4. De Blasio, F.V., Elverhøi, A., Issler, D., Harbitz, C.B., Bryn, P., and Lien, R., Flow models of natural debris flows originating from overconsolidated clay materials. *Marine Geology*, 2004. **213**(1–4): p. 439-455.
5. Locat, J. and Demers, D., Viscosity, yield stress, remolded strength, and liquidity index relationships for sensitive clays. *Canadian Geotechnical Journal*, 1988. **25**(4): p. 799-806.
6. Quinn, P.E., Diederichs, M.S., Rowe, R.K., and Hutchinson, D.J., Development of progressive failure in sensitive clay slopes. *Canadian Geotechnical Journal*, 2012. **49**(7): p. 782-795.
7. Bernander, S., Kullingsjö, A., Gylland, A.S., Bengtsson, P.-E., Knutsson, S., Pusch, R., Olofsson, J., and Elfgren, L., Downhill progressive landslides in long natural slopes: triggering agents and landslide phases modeled with a finite difference method. *Canadian Geotechnical Journal*, 2016. **53**(10): p. 1565-1582.
8. Wang, B., Vardon, P.J., and Hicks, M.A., Investigation of retrogressive and progressive slope failure mechanisms using the material point method. *Computers and Geotechnics*, 2016. **78**: p. 88-98.
9. Dey, R., Hawlader, B., Phillips, R., and Soga, K., Large deformation finite-element modelling of progressive failure leading to spread in sensitive clay slopes. *Géotechnique*, 2015. **65**(8): p. 657-668.
10. Dey, R., Hawlader, B.C., Phillips, R., and Soga, K., Numerical modelling of submarine landslides with sensitive clay layers. *Géotechnique*, 2016. **66**(6): p. 454-468.

11. Dey, R., Hawlader, B., Phillips, R., and Soga, K., Modeling of large-deformation behaviour of marine sensitive clays and its application to submarine slope stability analysis. *Canadian Geotechnical Journal*, 2016. **53**(7): p. 1138-1155.
12. Germanovich, L.N., Kim, S., and Puzrin, A.M., Dynamic growth of slip surfaces in catastrophic landslides. *Proceedings of the Royal Society A: Mathematical, Physical and Engineering Science*, 2016. **472**(2185).
13. Puzrin, A.M., Simple criteria for ploughing and runout in post-failure evolution of submarine landslides. *Canadian Geotechnical Journal*, 2016. **53**(8): p. 1305-1314.
14. Viesca, R.C. and Rice, J.R., Nucleation of slip-weakening rupture instability in landslides by localized increase of pore pressure. *Journal of Geophysical Research: Solid Earth*, 2012. **117**(B3): p. n/a-n/a.
15. Palmer, A.C. and Rice, J.R., The Growth of Slip Surfaces in the Progressive Failure of Over-Consolidated Clay. *Proceedings of the Royal Society of London. A. Mathematical and Physical Sciences*, 1973. **332**(1591): p. 527-548.
16. Puzrin, A.M. and Germanovich, L.N., The growth of shear bands in the catastrophic failure of soils. *Proceedings of the Royal Society A: Mathematical, Physical and Engineering Science*, 2005. **461**(2056): p. 1199-1228.
17. Puzrin, A.M., Germanovich, L.N., and Friedli, B., Shear band propagation analysis of submarine slope stability. *Géotechnique*, 2016. **66**(3): p. 188-201.
18. Reissner, E., On a variational theorem in elasticity. *Journal of Mathematical Physics*, 1950. **24**: p. 90-95.
19. Andersen, E.D., Roos, C., and Terlaky, T., On implementing a primal-dual interior-point method for conic quadratic optimization. *Mathematical Programming*, 2003. **95**(2): p. 249-277.
20. Sivaselvan, M.V., Complementarity framework for non-linear dynamic analysis of skeletal structures with softening plastic hinges. *International Journal for Numerical Methods in Engineering*, 2011. **86**(2): p. 182-223.
21. Krabbenhøft, K., Lyamin, A., and Sloan, S., Formulation and solution of some plasticity problems as conic programs. *International Journal of Solids and Structures*, 2007. **44**(5): p. 1533-1549.
22. Makrodimopoulos, A., Remarks on some properties of conic yield restrictions in limit analysis. *International Journal for Numerical Methods in Biomedical Engineering*, 2010. **26**(11): p. 1449-1461.
23. Zhang, X., Sheng, D., Sloan, S.W., and Krabbenhoft, K., Second-order cone programming formulation for consolidation analysis of saturated porous media. *Computational Mechanics*, 2016. **58**(1): p. 29-43.
24. Zhang, X., Ding, Y., Sheng, D., Sloan, S.W., and Huang, W., Quasi-static collapse of two-dimensional granular columns: insight from continuum modelling. *Granular Matter*, 2016. **18**(3): p. 1-14.
25. Zhang, X., Krabbenhoft, K., and Sheng, D., Particle finite element analysis of the granular column collapse problem. *Granular Matter*, 2014. **16**(4): p. 609-619.
26. Zhang, X., Krabbenhoft, K., Pedroso, D., Lyamin, A., Sheng, D., Da Silva, M.V., and Wang, D., Particle finite element analysis of large deformation and granular flow problems. *Computers and Geotechnics*, 2013. **54**: p. 133-142.
27. Oñate, E., Celigueta, M.A., Idelsohn, S.R., Salazar, F., and Suárez, B., Possibilities of the particle finite element method for fluid–soil–structure interaction problems. *Computational Mechanics*, 2011. **48**(3): p. 307-318.
28. Cremonesi, M., Frangi, A., and Perego, U., A Lagrangian finite element approach for the analysis of fluid-structure interaction problems. *International Journal for Numerical Methods in Engineering*, 2010. **84**(5): p. 610-630.
29. Zhang, X., Krabbenhoft, K., Sheng, D., and Li, W., Numerical simulation of a flow-like

landslide using the particle finite element method. *Computational Mechanics*, 2015. **55**(1): p. 167-177.

30. Salazar, F., Irazábal, J., Larese, A., and Oñate, E., Numerical modelling of landslide-generated waves with the particle finite element method (PFEM) and a non-Newtonian flow model. *International Journal for Numerical and Analytical Methods in Geomechanics*, 2016. **40**(6): p. 809-826.
31. Potts, D.M., Dounias, G.T., and Vaughan, P.R., Finite element analysis of progressive failure of Carsington embankment. *Géotechnique*, 1990. **40**(1): p. 79-101.
32. Troncone, A., Numerical analysis of a landslide in soils with strain-softening behaviour. *Géotechnique*, 2005. **55**(8): p. 585-596.
33. Krabbenhoft, K., Lyamin, A.V., Sloan, S.W., and Wriggers, P., An interior-point algorithm for elastoplasticity. *International Journal for Numerical Methods in Engineering*, 2007. **69**(3): p. 592-626.
34. Krabbenhoft, K. and Lyamin, A.V., Computational Cam clay plasticity using second-order cone programming. *Computer Methods in Applied Mechanics and Engineering*, 2012. **209–212**(0): p. 239-249.
35. Zhang, X., Krabbenhoft, K., Pedroso, D.M., Lyamin, A.V., Sheng, D., da Silva, M.V., and Wang, D., Particle finite element analysis of large deformation and granular flow problems. *Computers and Geotechnics*, 2013. **54**: p. 133-142.
36. Le, C.V., Nguyen-Xuan, H., and Nguyen-Dang, H., Upper and lower bound limit analysis of plates using FEM and second-order cone programming. *Computers & Structures*, 2010. **88**(1–2): p. 65-73.
37. Makrodimopoulos, A. and Martin, C.M., Upper bound limit analysis using simplex strain elements and second-order cone programming. *International Journal for Numerical and Analytical Methods in Geomechanics*, 2007. **31**(6): p. 835-865.
38. Makrodimopoulos, A. and Martin, C.M., Lower bound limit analysis of cohesive-frictional materials using second-order cone programming. *International Journal for Numerical Methods in Engineering*, 2006. **66**(4): p. 604-634.
39. Yonekura, K. and Kanno, Y., Second-order cone programming with warm start for elastoplastic analysis with von Mises yield criterion. *Optimization and Engineering*, 2012. **13**(2): p. 181-218.
40. Zhang, X., Sheng, D., Kouretzis, G.P., Krabbenhoft, K., and Sloan, S.W., Numerical investigation of the cylinder movement in granular matter. *Physical Review E*, 2015. **91**(2): p. 022204.
41. Bleyer, J., Maillard, M., de Buhan, P., and Coussot, P., Efficient numerical computations of yield stress fluid flows using second-order cone programming. *Computer Methods in Applied Mechanics and Engineering*, 2015. **283**: p. 599-614.
42. Huang, J., da Silva, M.V., and Krabbenhoft, K., Three-dimensional granular contact dynamics with rolling resistance. *Computers and Geotechnics*, 2013. **49**: p. 289-298.
43. Krabbenhoft, K., Huang, J., da Silva, M.V., and Lyamin, A.V., Granular contact dynamics with particle elasticity. *Granular Matter*, 2012. **14**(5): p. 607-619.
44. Krabbenhoft, K., Lyamin, A.V., Huang, J., and Vicente da Silva, M., Granular contact dynamics using mathematical programming methods. *Computers and Geotechnics*, 2012. **43**: p. 165-176.
45. Oñate, E., Idelsohn, S.R., Del Pin, F., and Aubry, R., The Particle Finite Element Method - An Overview. *International Journal of Computational Methods*, 2004. **01**(02): p. 267-307.
46. Cremonesi, M., Frangi, A., and Perego, U., A Lagrangian finite element approach for the simulation of water-waves induced by landslides. *Computers & Structures*, 2011. **89**(11–12): p. 1086-1093.
47. Edelsbrunner, H., M, E.P., #252, and cke, Three-dimensional alpha shapes. *ACM Trans. Graph.*, 1994. **13**(1): p. 43-72.

48. Dávalos, C., Cante, J., Hernández, J.A., and Oliver, J., On the numerical modeling of granular material flows via the Particle Finite Element Method (PFEM). *International Journal of Solids and Structures*, 2015. **71**: p. 99-125.

49. Cante, J., Dávalos, C., Hernández, J.A., Oliver, J., Jonsén, P., Gustafsson, G., and Häggblad, H.Å., PFEM-based modeling of industrial granular flows. *Computational Particle Mechanics*, 2014. **1**(1): p. 47-70.

50. Cremonesi, M., Ferri, F., and Perego, U., A basal slip model for Lagrangian finite element simulations of 3D landslides. *International Journal for Numerical and Analytical Methods in Geomechanics*, 2016: p. n/a-n/a.

51. Becker, P., Idelsohn, S.R., and Oñate, E., A unified monolithic approach for multi-fluid flows and fluid–structure interaction using the Particle Finite Element Method with fixed mesh. *Computational Mechanics*, 2015. **55**(6): p. 1091-1104.

52. Idelsohn, S.R., Mier-Torrecilla, M., Marti, J., and Oñate, E., *The Particle Finite Element Method for Multi-Fluid Flows*, in *Particle-Based Methods: Fundamentals and Applications*, E. Oñate and R. Owen, Editors. 2011, Springer Netherlands: Dordrecht. p. 135-158.

53. Idelsohn, S., Mier-Torrecilla, M., and Oñate, E., Multi-fluid flows with the Particle Finite Element Method. *Computer Methods in Applied Mechanics and Engineering*, 2009. **198**(33–36): p. 2750-2767.

54. Zhu, M. and Scott, M.H., Improved fractional step method for simulating fluid-structure interaction using the PFEM. *International Journal for Numerical Methods in Engineering*, 2014. **99**(12): p. 925-944.

55. Cremonesi, M., Frangi, A., and Perego, U., A Lagrangian finite element approach for the analysis of fluid–structure interaction problems. *International Journal for Numerical Methods in Engineering*, 2010. **84**(5): p. 610-630.

56. Mier-Torrecilla, M., Idelsohn, S.R., and Oñate, E., Advances in the simulation of multi-fluid flows with the particle finite element method. Application to bubble dynamics. *International Journal for Numerical Methods in Fluids*, 2011. **67**(11): p. 1516-1539.

57. Oñate, E., Rossi, R., Idelsohn, S.R., and Butler, K.M., Melting and spread of polymers in fire with the particle finite element method. *International Journal for Numerical Methods in Engineering*, 2010. **81**(8): p. 1046-1072.

58. Cremonesi, M., Ferrara, L., Frangi, A., and Perego, U., Simulation of the flow of fresh cement suspensions by a Lagrangian finite element approach. *Journal of Non-Newtonian Fluid Mechanics*, 2010. **165**(23–24): p. 1555-1563.

59. Zhang, X., *Particle finite element method in geomechanics*, in *PhD Thesis*. 2014.

60. Hu, Y. and Randolph, M.F., A practical numerical approach for large deformation problems in soil. *International Journal for Numerical and Analytical Methods in Geomechanics*, 1998. **22**(5): p. 327-350.

61. Tian, Y., Cassidy, M.J., Randolph, M.F., Wang, D., and Gaudin, C., A simple implementation of RITSS and its application in large deformation analysis. *Computers and Geotechnics*, 2014. **56**: p. 160-167.

62. Needleman, A., Material rate dependence and mesh sensitivity in localization problems. *Computer Methods in Applied Mechanics and Engineering*, 1988. **67**(1): p. 69-85.

63. Prevost, J.H. and Loret, B., Dynamic strain localization in elasto-(visco-)plastic solids, part 2. plane strain examples. *Computer Methods in Applied Mechanics and Engineering*, 1990. **83**(3): p. 275-294.

64. Moore, I.D. and Rowe, R.K., Numerical models for evaluating progressive failure in earth structures—A review. *Computers and Geotechnics*, 1988. **6**(3): p. 217-239.

65. Andrade, J.E., Avila, C.F., Hall, S.A., Lenoir, N., and Viggiani, G., Multiscale modeling and characterization of granular matter: From grain kinematics to continuum mechanics. *Journal of the Mechanics and Physics of Solids*, 2011. **59**(2): p. 237-250.

66. Li, X., Zhang, X., and Zhang, J., A generalized Hill's lemma and micromechanically based

macroscopic constitutive model for heterogeneous granular materials. *Computer Methods in Applied Mechanics and Engineering*, 2010. **199**(49–52): p. 3137-3152.

67. Guo, N. and Zhao, J., A coupled FEM/DEM approach for hierarchical multiscale modelling of granular media. *International Journal for Numerical Methods in Engineering*, 2014. **99**(11): p. 789-818.
68. Li, X., Zhang, J., and Zhang, X., Micro-macro homogenization of gradient-enhanced Cosserat media. *European Journal of Mechanics - A/Solids*, 2011. **30**(3): p. 362-372.
69. De Souza Neto, E.A., Peric, D., and Owen, D.R.J., *Computational Methods for Plasticity: Theory and Applications*. 2008: John Wiley.
70. Lube, G., Huppert, H.E., Sparks, R.S.J., and Freundt, A., Collapses of two-dimensional granular columns. *Physical Review E*, 2005. **72**(4).
71. Lajeunesse, E., Monnier, J.B., and Homsy, G.M., Granular slumping on a horizontal surface. *Physics of Fluids*, 2005. **17**(10).
72. Balmforth, N.J. and Kerswell, R.R., Granular collapse in two dimensions. *Journal of Fluid Mechanics*, 2005. **538**: p. 399-428.
73. Thompson, E.L. and Huppert, H.E., Granular column collapses: further experimental results. *Journal of Fluid Mechanics*, 2007. **575**: p. 177-186.
74. Lacaze, L., Phillips, J.C., and Kerswell, R.R., Planar collapse of a granular column: Experiments and discrete element simulations. *Physics of Fluids*, 2008. **20**(6).
75. Edgers, L. and Karlsrud, K., Soil flows generated by submarine slides - case studies and consequences. *Norwegian Goetechnical Institute, Publication*, 1982(143): p. 1-10.
76. Johnson, A.M. and Rodine, J.R., *Debris flow*, in *Slope instability*, D. Brunsden and D.B. Prior, Editors. 1984, Wiley: New York. p. 257-362.

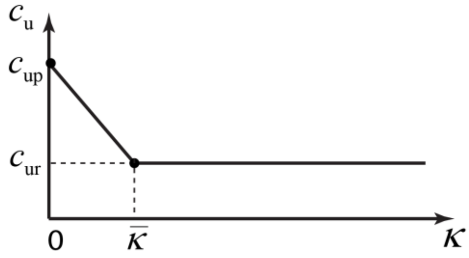

Figure 1. Variation of c_{u} with deviatoric plastic strain represented by parameter κ

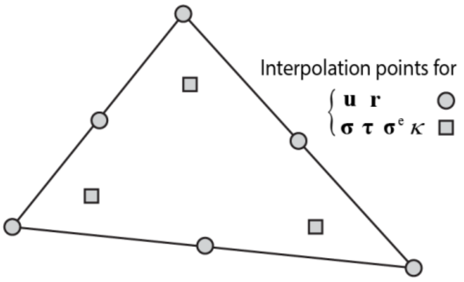

Figure 2. The mixed triangular element used in the simulation

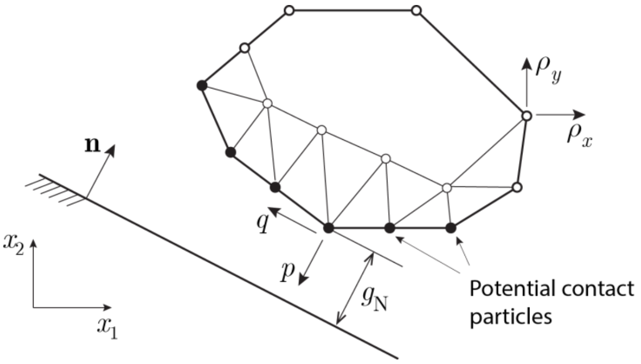

Figure 3. The contact between a deformable body and a rigid surface

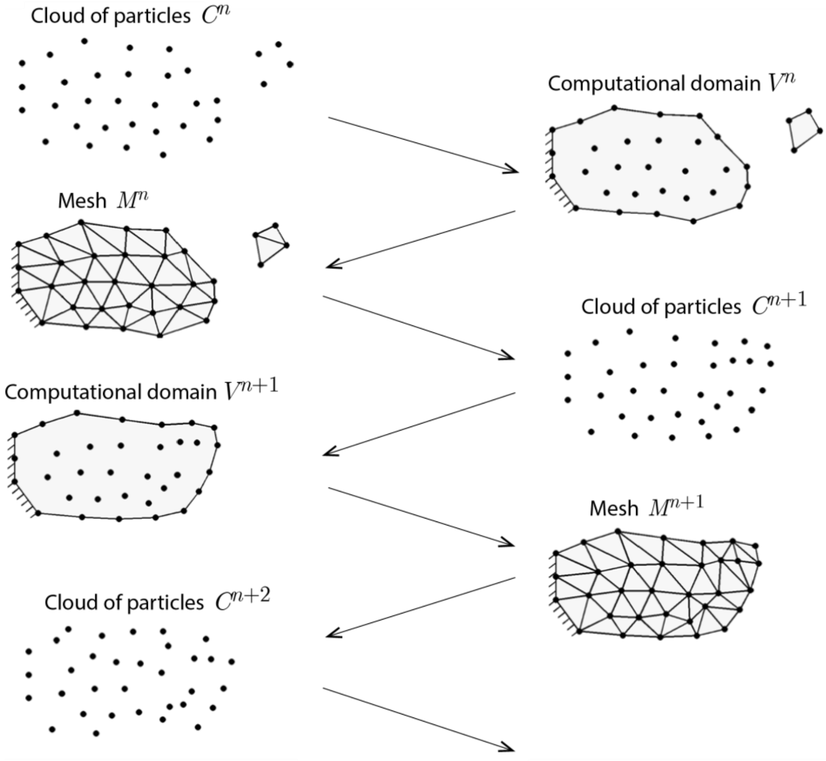

Figure 4. Steps for the Particle Finite Element Method (after [35])

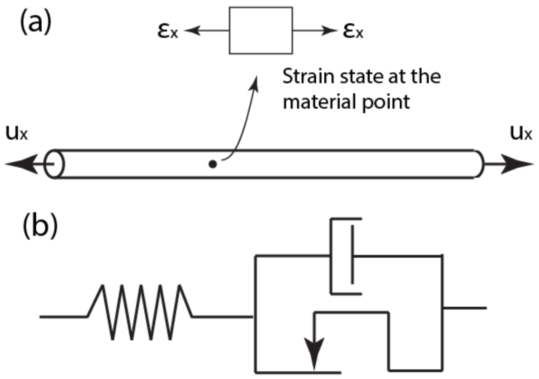

Figure 5. (a) Schematic diagram of a bar subject to uniaxial loads; and (b) one-dimensional elastoviscoplastic model.

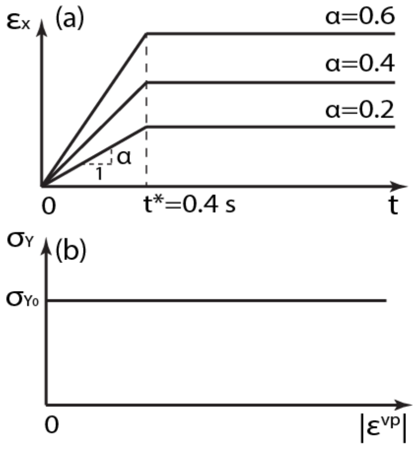

Figure 6. Curves of (a) the applied strain rate and (b) the variation of the yield stress for the one-dimensional stress relaxation problem

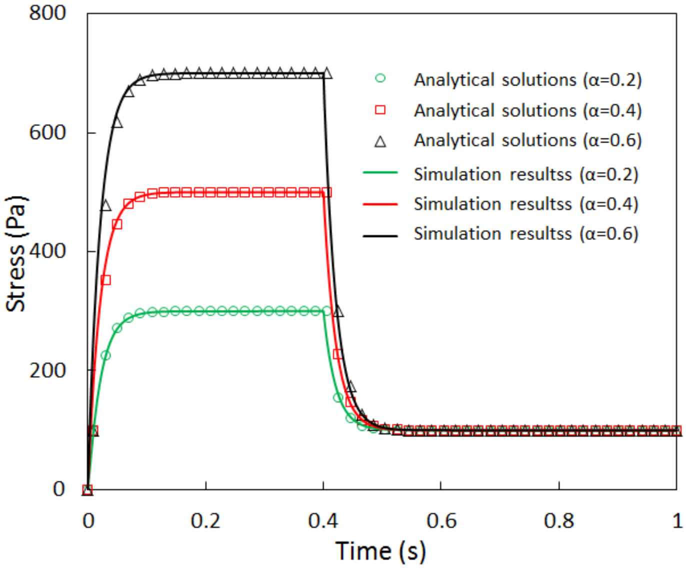

Figure 7. Comparison of numerical and analytical solutions for the one-dimensional stress relaxation problem

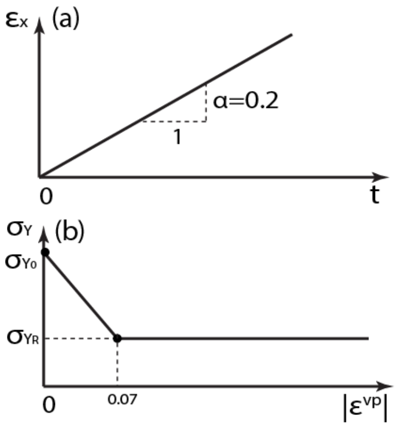

Figure 8. Curves of (a) the applied strain rate and (b) the variation of the yield stress for the one-dimensional strain-softening problem

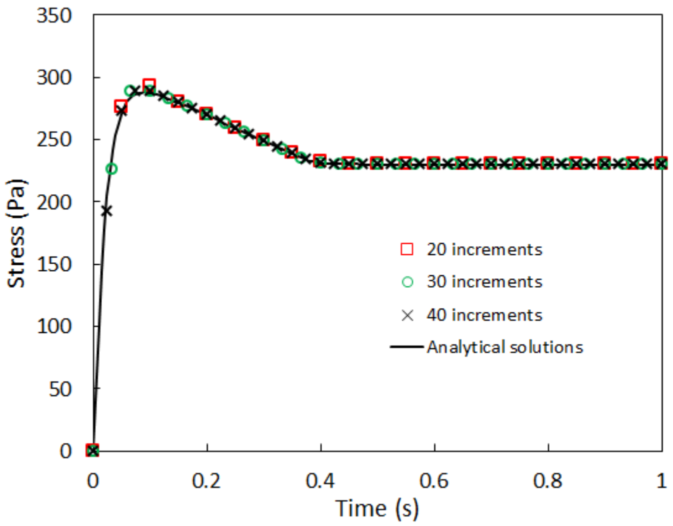

Figure 9. Comparison of numerical and analytical solutions for the one-dimensional elastoviscoplastic problem with strain softening

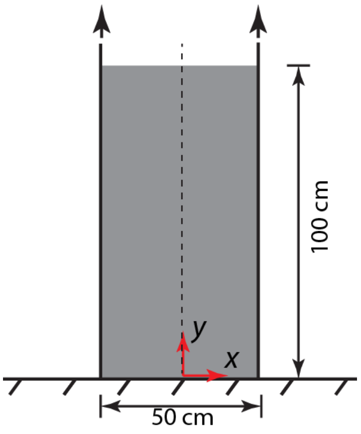

Figure 10. Schematic diagram for the collapse of a column of sensitive clays

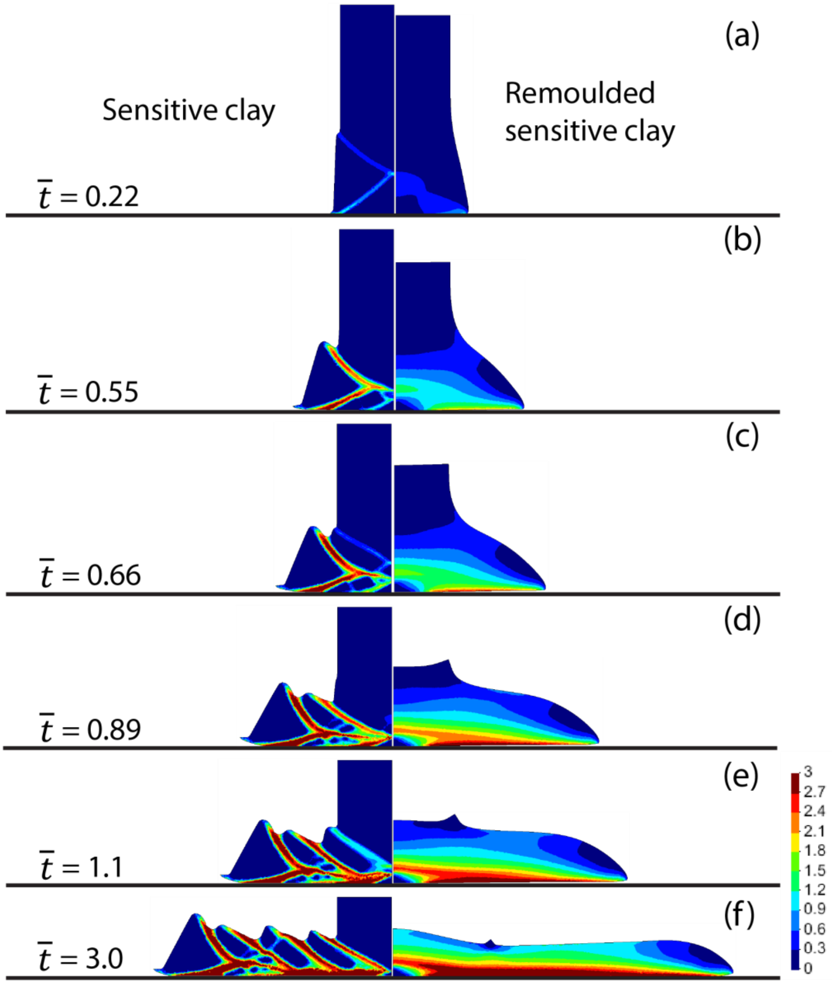

Figure 11. Collapse evolution processes of the column of initially undisturbed sensitive clays and remoulded sensitive clays. Colours are proportional to accumulated equivalent plastic strain

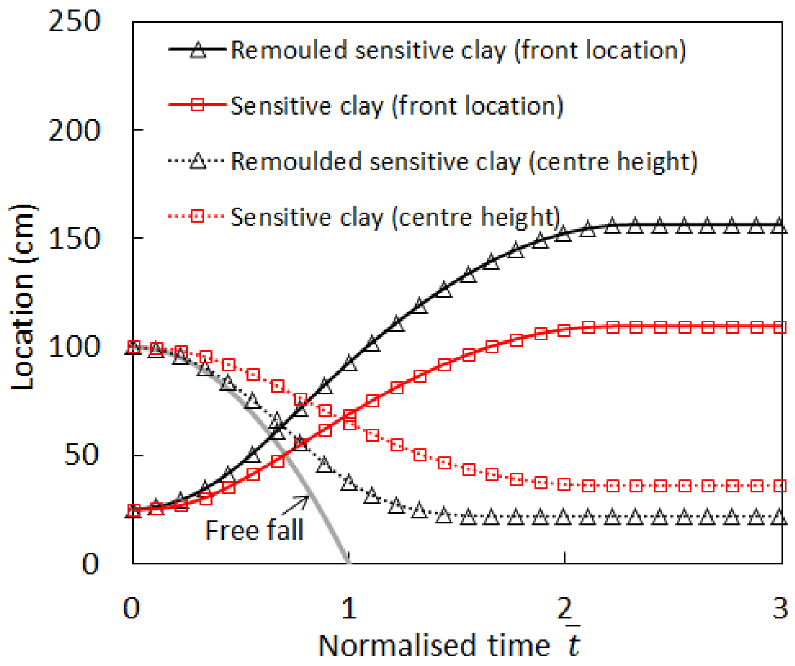

Figure 12. Curves of the front location and the centre height of the column against normalized time

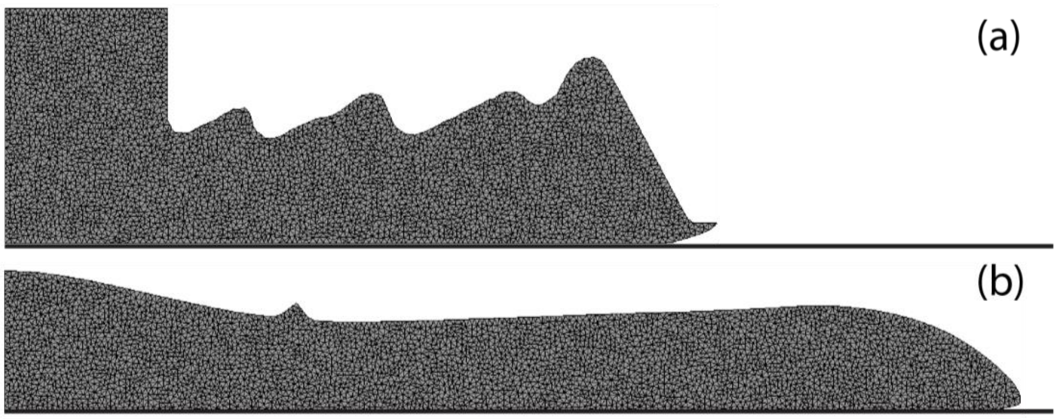

Figure 13. Final configuration with mesh topology illustrated

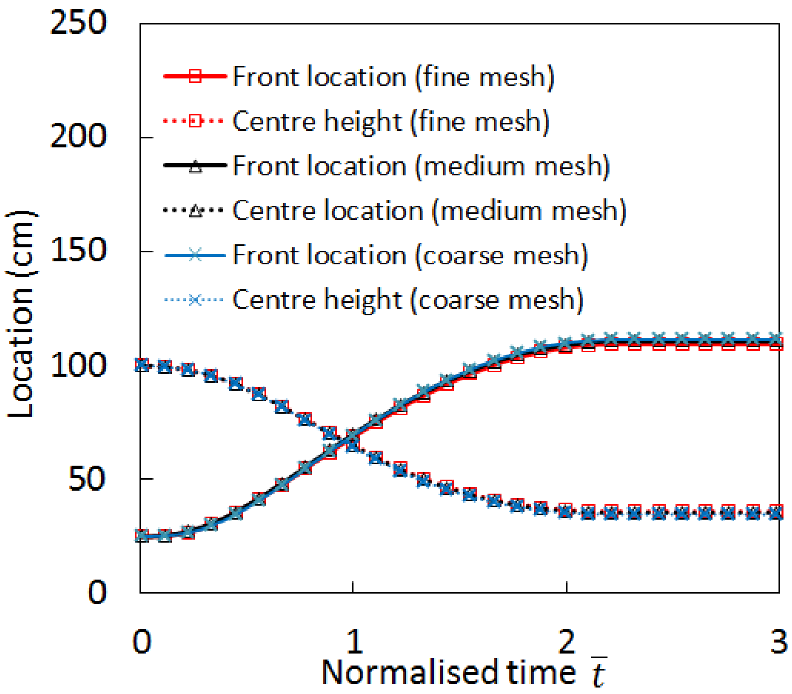

Figure 14. Effects of the utilized mesh size on the curves for front location and centre height of the column against normalized time

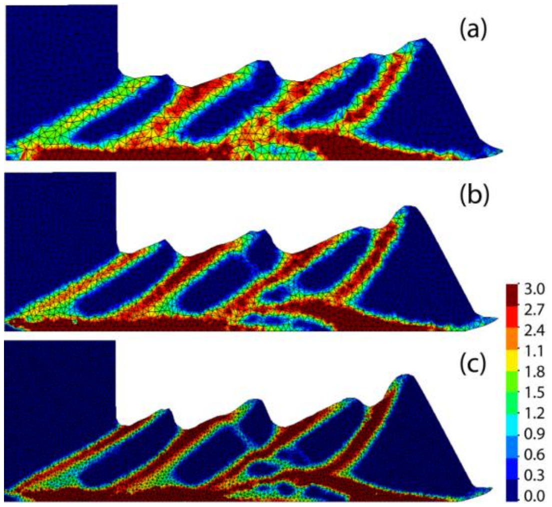

Figure 15. Final configurations and shear band distributions of the column collapse using (a) coarse meshes, (b) medium meshes, and (c) fine meshes. Colours are proportional to the accumulated equivalent plastic strain

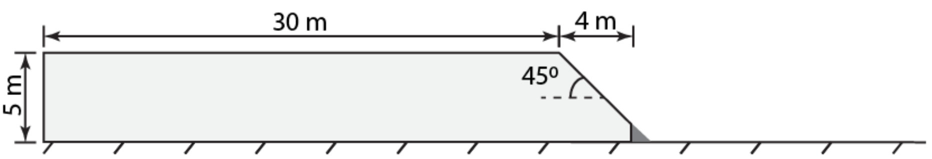

Figure 16. Schematic diagram for the retrogressive failure of a slope in sensitive clays.

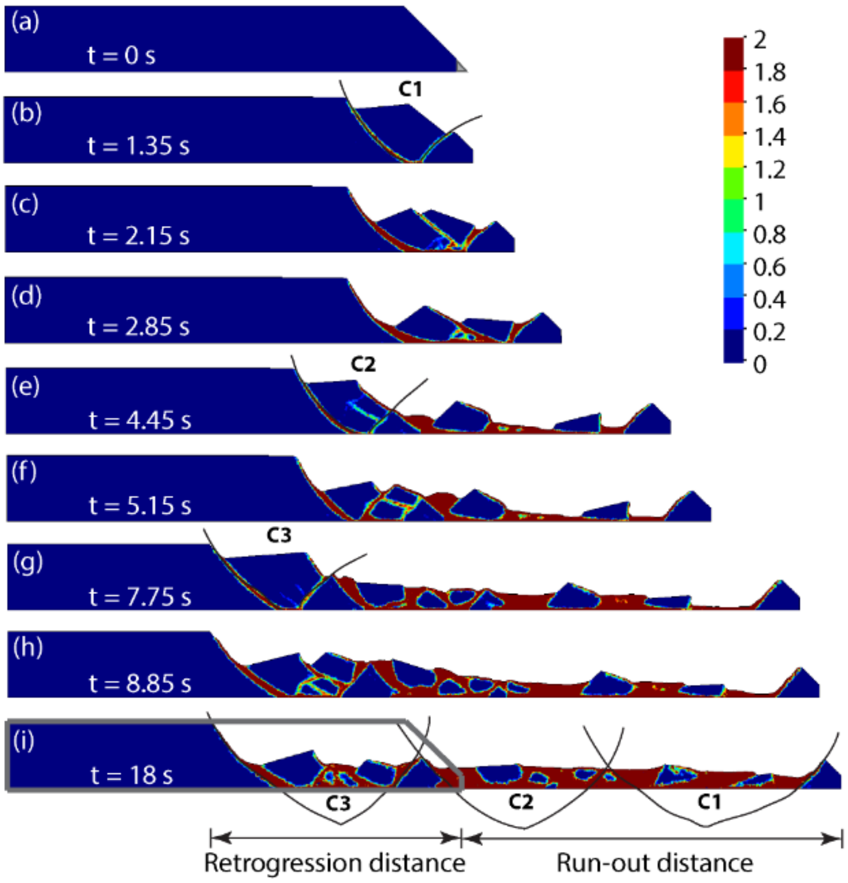

Figure 17. Retrogressive failure procedures of the slope. Colours are proportional to accumulated equivalent plastic strain

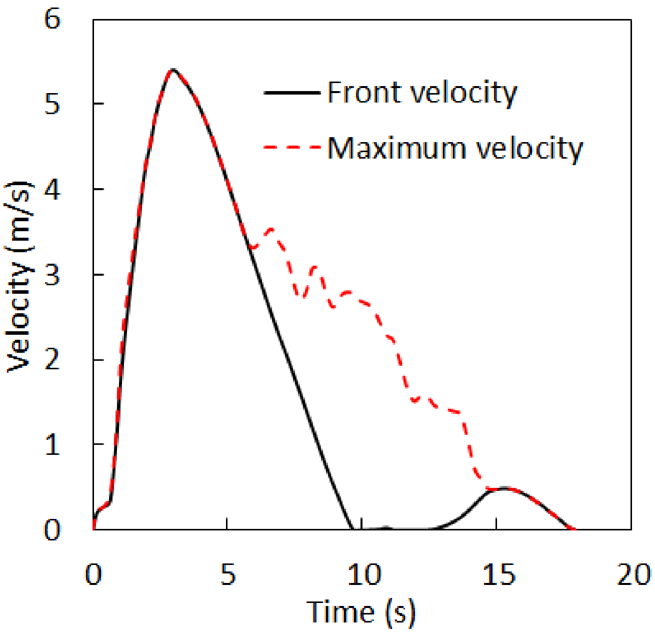

Figure 18. Velocity of the sliding front and the maximum velocity against time

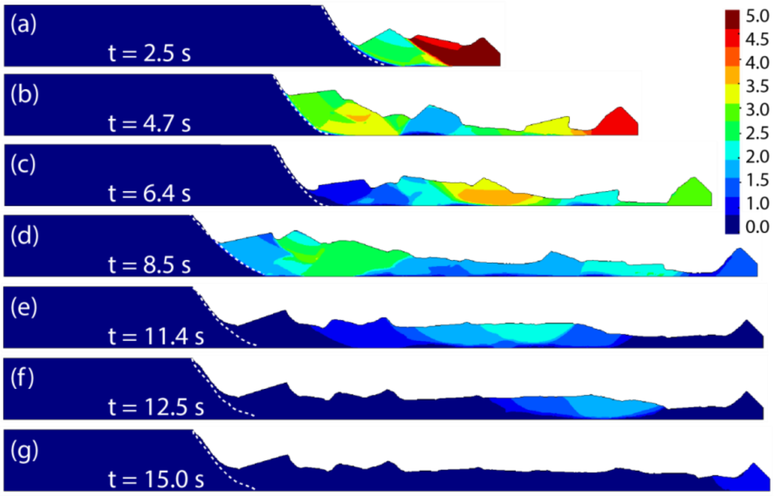

Figure 19. Velocity contour during the retrogressive failure

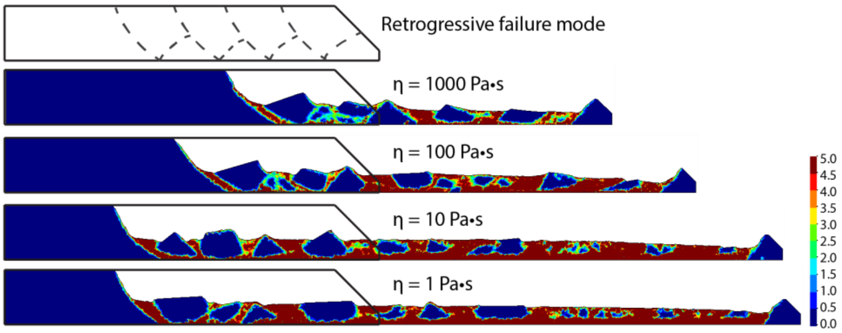

Figure 20. Final deposits from the simulation using different viscosity coefficients for sensitive clays

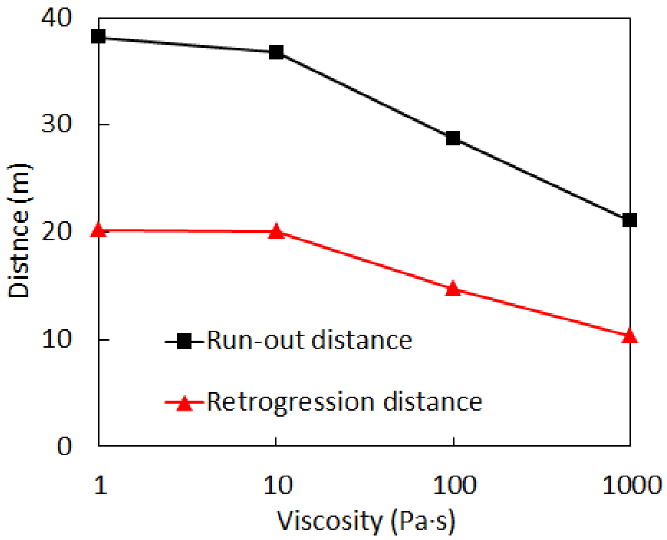

Figure 21. Curves of run-out distance and retrogression distance against viscosity